



POZNAN UNIVERSITY OF TECHNOLOGY

FACULTY OF COMPUTING AND TELECOMMUNICATIONS

Institute of Radiocommunications

Bachelor's thesis

**ANGLE OF ARRIVAL ESTIMATION IN MULTI-ANTENNA
SOFTWARE DEFINED RADIO SYSTEM: FROM DESIGN TO
EVALUATION**

Marcin Wachowiak, 135670

Supervisor
dr inż. Paweł Kryszkiewicz

POZNAŃ 2021

Streszczenie

Wraz z rozwojem sieci komórkowych pojawiają się nowe metody efektywnego wykorzystania widma bazujące na wielodostępie przestrzennym. Coraz częściej stosowane macierze antenowe pozwalają na selektywną zmianę charakterystyk promieniowania co umożliwia zestawienie dedykowanych kanałów radiowych. Dla efektywnego wykorzystania możliwości systemu ze sterowanymi wiązkami konieczne jest wyznaczenie lokalizacji użytkownika lub kąta nadajścia sygnału. W pracy przedstawiona jest analiza algorytmu Multiple signal classification (MUSIC) zastosowanego celu wykrycia kierunku nadajścia sygnału radiowego z wykorzystaniem liniowej macierzy antenowej. Przedstawiona zostaje metoda synchronizacji faz przebiegów za pomocą kanału radiowego i krótkiego okresu kalibracji. Testy algorytmu w rzeczywistym środowisku radiowym przeprowadzone za pomocą GNU Radio oraz platformy radia programowalnego USRP B210 pozwalają na weryfikację funkcjonalności systemu. Porównując uzyskane wyniki z symulacjami zaproponowane zostają metody redukujące wrażliwość algorytmu na niedoskonałości realizacji sprzętowej. Zastosowana filtracja pasmowo-przepustowa pozwala na poprawienie dokładności kalibracji systemu oraz wykluczenie źródeł zakłócających. Dodatkowe aktywne przetwarzanie za pomocą ruchomej średniej pozwala zredukować wariancję wyników. Weryfikacja systemu w rzeczywistych warunkach radiowych, pozwala na określenie potencjalnych zastosowań oraz ocenę zaproponowanych rozwiązań.

Abstract

The ever-growing demand for capacity in cellular networks has brought about novel methods of frequency reuse one of which is spatial multiplexing. Beamforming employed in massive phased arrays enables establishment of dedicated spatial RF channels resulting in significant performance improvement. Steering of the beam is facilitated by known user location or signals direction of arrival. This work presents an analysis of Multiple signal classification (MUSIC) algorithm applied to estimate direction of arrival of RF signal using uniform linear array. Based on available publications and sources a few methods of device synchronization and calibration are presented. An approach of phase synchronization using wireless channel and short calibration interval is proposed and tested. Setup evaluation is performed in GNU Radio environment with the use of USRP B210 software defined radio platform. Conclusions drawn from tests in real radio environment result in modifications improving the accuracy of the algorithm. Introduced band-pass filtering offers an increase in stability and precision of calibration procedure. It is also capable of attenuating unwanted signals in order to exclude interference from distorting the estimation results. Testing performed within this work serves as a verification to proposed enhancements. Moreover, encountered hardware, medium and algorithm limitations are noted and discussed thoroughly.

Contents

1	Introduction	1
1.1	Importance of Wireless Communications	1
1.2	Key enabling technologies of the newest and future mobile networks	3
1.3	User localization in cellular networks	4
1.4	Aims and objectives	6
2	AoA estimation: state of the art in algorithms and SDR-based implementations	7
2.1	Algorithms for angle estimation	7
2.2	Signal and noise subspaces in the context of uniform linear array	8
2.3	Multiple Signal Classification based method of direction of arrival estimation	12
2.4	Synchronization and calibration	15
2.5	Literature review	16
3	Implementation	19
3.1	Algorithm simulation	19
3.2	Hardware and software environment	24
3.3	Implemented signal processing blocks	29
3.4	Flowgraph scenarios	32
3.5	Wireless calibration routine	36
4	Measurements	39
4.1	Stability of phase calibration	39
4.2	Accuracy evaluation	43
4.3	Field tests	46
5	Summary	49
5.1	Conclusion	49
5.2	Future work	50
	Acronyms	51
	Bibliography	53

Chapter 1

Introduction

1.1 Importance of Wireless Communications

The idea of wireless connectivity in a form of radio link has undergone a prolonged evolution. From the very beginning radio waves have been employed to communicate information over great distances. First in a way of broadcasts of sound, then came the television. After some time the cellular networks were introduced. Enabling consumers to perform calls almost anywhere they found suitable. From that moment on, the range of offered services has been ceaselessly extended. Users quickly appreciated the comforts of mobility and the advances in hardware encouraged new generations of wireless networks. Another surge in popularity of mobile services falls on the Information Age which started with the growing popularity of the Internet. Advances in scale of integration of semiconductor devices enabled commercialization of smartphones - mobile computing devices with broadband wireless access. The technical definition of smartphone is far from what it is associated with in everyday life. Serving as a personal computer with functions varying from simple voice calls to high quality video streaming it has become an essential device.

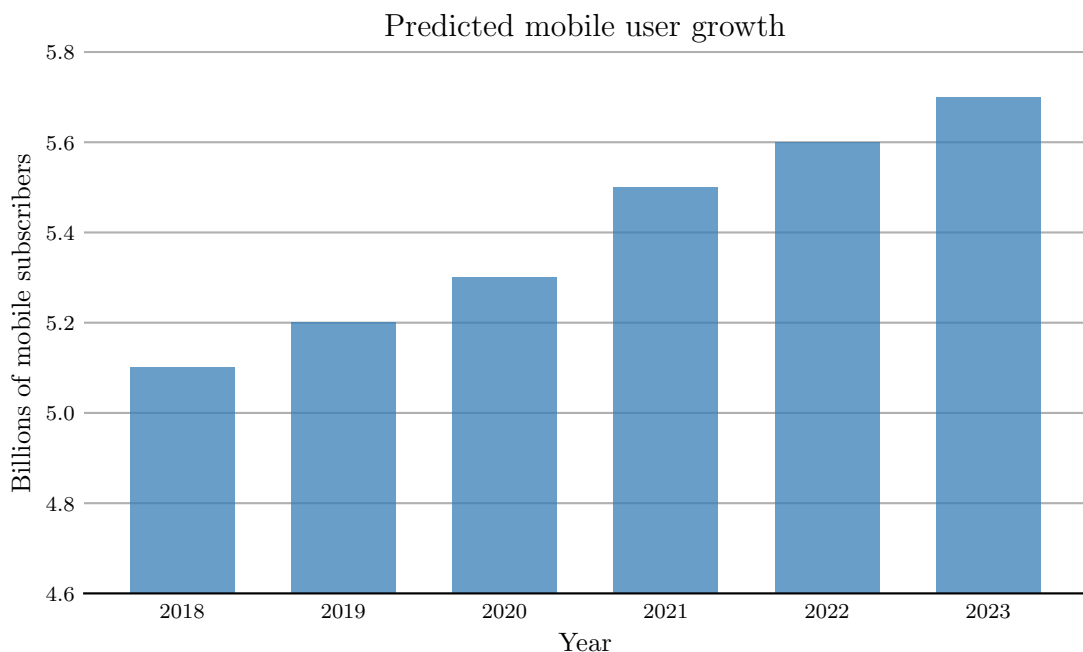


Figure 1.1: Mobile user growth according to Cisco Annual Internet Report 2018-2023 [3].

The demand for mobile data seems insatiable, on the other hand resources providing it are limited. According to [3] number of mobile network users will continue to steadily grow approximately 100 million each year as can be seen in Fig. 1.1. Mobile subscriber penetration rate is expected to increase from 66% in 2018 to 71% in 2023. Total sum of users is forecasted to slow down and stabilise due to saturation of the market. Greater density of user equipment to serve is also troubling, but it is the throughput requirements that pose the major challenge to the future mobile networks.

As the technology advances, more immersive forms of mobile entertainment emerge, for example extended reality or 360° UHD video streaming. Latest generations of mobile networks aim to enable time critical communications that include reliable industrial motion control as well as mobility cooperation. These applications are data intensive and require significant bit rates as well as low latency and ultra high reliability, which profoundly affect the Quality of Service. Subsequently the demand for throughput is anticipated to follow the current trend of doubling each 2 years [12] as illustrated in Fig. 1.2. It is also worthy of notice that by the year 2026 fifth generation of cellular networks is expected to handle 54% of total mobile data.

Such surge in capacity is also fueled by the deployment of Massive IoT that will rely on 5G networks and LTE-M. Rolling out of cellular IoT in its current phase may appear stagnant, however the time of deployment is yet to come. As reported by [12] currently there are about 1,6 billion of cellular IoT connections, which number is estimated to double each 3 years to achieve value of 6 billion in 2026.

Overall, the advancing technology is supposed to force area throughput improvement by a factor of 1000 [17]. Increase of such order requires novel approach to efficient spectrum utilization and development of complex network hierarchy. Densification of networks may require new solutions in regard to security and optimization of power consumption of the devices. Whereas, the exact moment of achieving this milestone remains unknown, novel network generations are introduced to satisfy the demand.

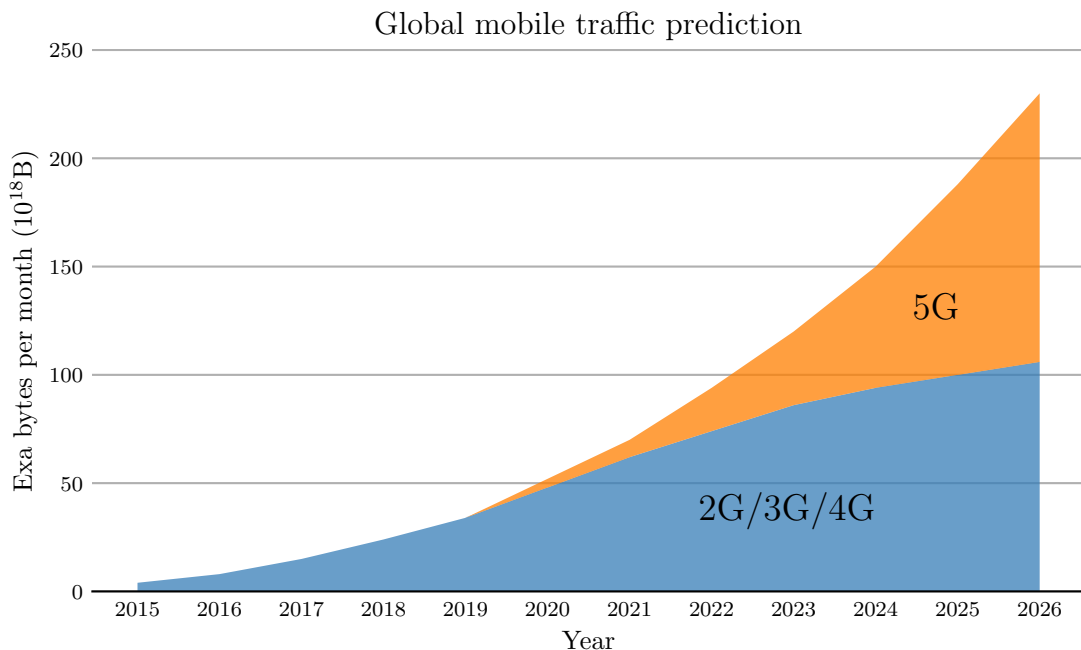


Figure 1.2: Global mobile data traffic prediction according to Ercisson Mobility Report 2020 [12].

Currently introduced 5G offers a few of distinguishable features over the 4th generation according to ITU-R recommendation [27]:

- User experienced data rate of 100 Mbit/s and peak data rate of 20 Gbit/s
- 100x better network energy efficiency, 10x prolonged battery life and 3x better spectrum efficiency
- Latency of 1ms and mobility up to 500 km/h
- Area traffic capacity of 10 Mbit/s/m² (1000x more than before)
- Up to 1 billion of connected devices per square kilometer

1.2 Key enabling technologies of the newest and future mobile networks

Predetermined features of next generation of mobile networks require ingenious solutions to facilitate the anticipated data rates, area capacity along with efficiency. As every complex infrastructure, future networks like 5G have a list of key enabling technologies and approaches [5],[2],[13]:

- Ultra densification of currently present cellular networks accompanied with excessive introduction of small cells. Focus on provisioning direct communications in peer-to-peer (P2P), device-to-device (D2D), machine-to-machine (M2M) schemes.
- Multi User Massive (MIMO) technology employing antenna arrays at the both ends of transmit chain. Antenna arrays may be utilized to introduce space-division multiple access (SDMA) based on separately encoded data streams. Moreover, MIMO facilitates beamforming, which relies on adaptive control of each antenna element coefficients to shape the beam enabling more directive communications.
- Application of millimeter wave frequencies as new communication bands. Unlicensed or unexploited high frequency bands starting from 24GHz provide great amount of spectrum required for expected data rates. Major obstacle of employing higher bands is attenuation, that limits the range of communications to a few hundred meters in line of sight propagation.
- Wireless software-defined networking, virtualization of wireless resources and cloud computing at the edge for better management of resources and cooperation. Idea of edge computing is to reduce the bandwidth and latency by providing data and processing power closest to

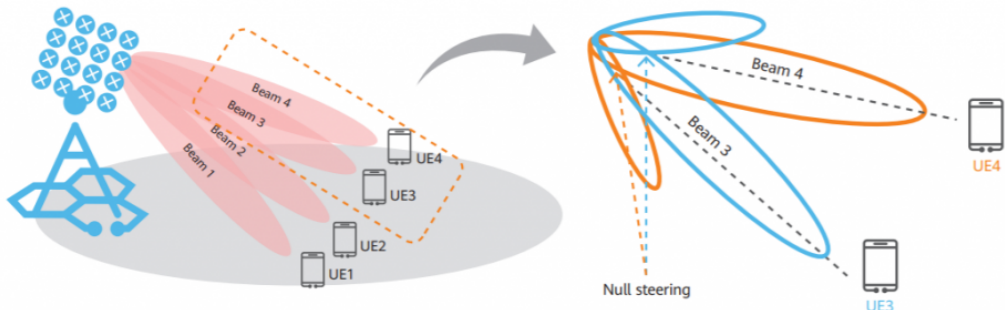


Figure 1.3: Illustrative drawing of beamforming – shaping the transmit beams to spatially separated users [source: <https://blog.huawei.com/>].

the point of interaction. In such scenario communication with distant data centers is reduced to minimum.

- Green communications based on energy harvesting or renewable resources for example wake-up radios. Energy-aware communication schemes like simultaneous wireless information and power transfer (SWIPT) or intelligent reflecting surface (IRS) .

From the aforementioned technologies Massive MIMO associated with beamforming appears to be especially feasible in the context of future networks and pushing limitations of the physical layer. Microwave frequency range encourages the usage of MIMO arrays, due to the reduced patch antenna sizes and possibility of overcoming high attenuation with focused beams. As proven in [21] when both sides of transmit chain use beamforming path loss exponents for mmW LOS scenario are similar to those of typical cellular bands due to combined effective antenna gain.

1.3 User localization in cellular networks

Efficient management of radio resources, which vary depending on location, to a certain degree requires information about actual user position. In the light of densification of network structure and applying novel frequency reuse schemes, estimation of user coordinates has become of greater importance. Base station (BS) – a radio transceiver serving as a hub of the wireless network, which utilizes beamforming in a way provides a location based service. The quality of service greatly depends on accuracy of estimation of user equipment (UE) coordinates to accordingly steer the transmit or receive beam. Depending on whether position is to be determined in plane or space, from 2 to 3 base stations are required to cooperate. Some of the most common methods of location estimation include [28]:

- Time of arrival (ToA) – distance from receiving station is estimated basing on the absolute time of arrival. With known signal velocity position can be determined basing on intersection of 3 circles marking distance from each RX station calculated from measured time of flight. Both UE and BS are required to be perfectly synchronized. Signal path between devices should be LOS, if it is otherwise the method introduces severe location errors. Accuracy depends on available bandwidth, that ensures timing resolution.
- Time difference of arrival (TDoA) – UE broadcasts a tag message with a timestamp. Receiving stations compare the times of arrival and employ multilateration to estimate position

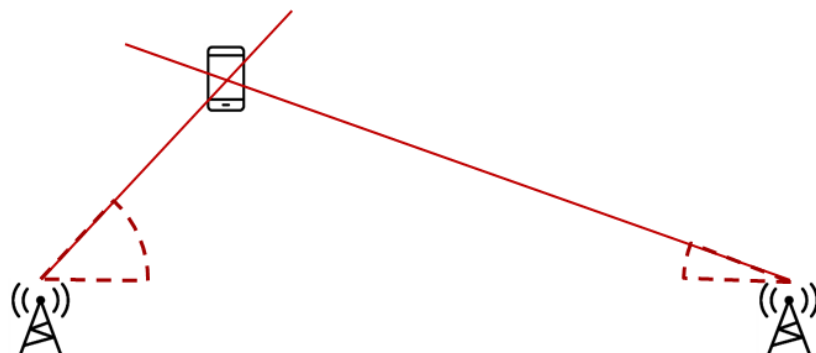


Figure 1.4: Location estimation based on AoA triangulation [source: www.ti.com].

of the device. Only the BSs are required to have clocks and time base synchronized as this method relies on the offset between times of reception at each spatially separated BS.

- Angle of arrival (AoA) – signals received by an antenna array are processed by appropriate estimation algorithm. Angles obtained by different BSs are triangulated using trigonometric identities to extract UE coordinates.
- Received signal strength (RSS) – each BS measures received signal power. Distance from each station is calculated from observed path loss in accordance to selected empirical channel model. Does not require synchronization and is cost-effective due to simplicity. In case of NLOS estimation detailed environmental propagation model is required.
- GPS assisted methods – depend on accuracy and availability of GPS localization as well as relevance of provided models of the surrounding environment. Inadequate for indoor estimation due to high attenuation of signal and low overall accuracy.
- FP – fingerprinting or DB – database correlation techniques. In the first offline phase the received signal strength indication (RSSI) is observed at different reference points in the area, and saved to the database. The second phase is active estimation of location based on actual RSSI and evaluation of the saved results. Suitable for indoor applications.

Most of above-mentioned methods assume that coordinates of BSs are perfectly known, which coincides with common practices. With growing presence of MIMO arrays, AoA estimation will probably become more widespread. However, the angle-of-arrival detection is susceptible to reflections of signal, that in some NLOS cases may introduce a critical error. Significance of the miscalculation varies depending on whether the estimation main aim was to locate the device or the direction of the strongest signal.

Regarding the concept of angle-of-arrival location estimation in the domain of mmW most cases assume LOS communications because of high attenuation and poor propagation properties. As suggested by simulations in [1] systems relying on such high frequencies and AoA detection are capable of localizing UE with sub-meter position error and sub-degree orientation error. The accuracy greatly depends on number of antenna elements and increases with the count.

Growing omnipresence of precise location estimation algorithms may facilitate prevalence of interactive forms of services or marketing. One may imagine possibilities like assisted sightseeing in historical areas or museums, shopping racks with proximity based advertising or assistance in commuting. Main advantage of cellular based precise localization services is that they do not require user to scan any codes as determined location associated with predefined map is sufficient to provide marketing information.

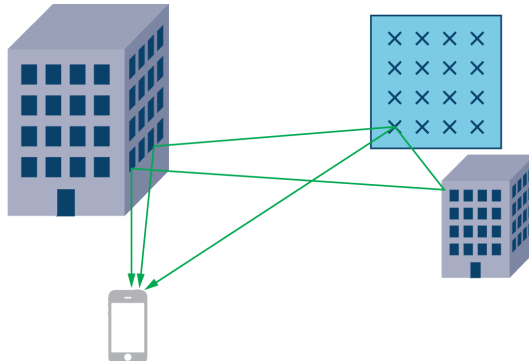


Figure 1.5: Reflected signal paths diagram [source: www.analog.com].

1.4 Aims and objectives

Aim of this work is to assemble a multi antenna software defined radio system capable of estimating angle of arrival and evaluate its performance. What is more, solutions minimizing limitations imposed by hardware, radio environment or nature of the algorithm will be discussed and tested.

Objectives:

- Radio system will be built using USRP B210 software-defined radio platform, which was not yet so broadly applied in angle estimation systems. The hardware will be operated via GNU Radio environment.
- Signal processing blocks and routines required for the evaluation will be implemented in C++ in GNU Radio framework and made accessible to anyone willing to replicate the results.
- The antenna array will be designed for 2.4–2.5 GHz ISM band and phase synchronized via wireless channel within a short period of time. Implementation of the method will enable recurrent calibration routine without the need to change wiring or switch channels.
- Accuracy of the phase synchronization as well as angle estimation will be enhanced by band-pass filtering of signals and moving average filtering of results. Applied filtering to isolate signal of interest has not yet been widely analyzed in the context of AoA estimation.
- Completed setup will be thoroughly tested in real radio environment and parametric analysis will serve to evaluate its performance. Proposed calibration and enhancements efficiency will be discussed basing on collected data representations and simulations.

Structure of the work

The rest of this paper is structured as follows, second chapter starts with survey resulting in comparison of AoA algorithms. Then the mathematical foundations of MUSIC algorithm are described along with its features and constraints. Section finishes with comment on devices synchronization methods. Third chapter begins with simulation of algorithm and parametric analysis. Next, method of system implementation in GNU Radio environment is depicted, followed by description of introduced signal processing blocks, created flowgraphs and a note about hardware equipment capabilities. Fourth chapter is dedicated to measurements of accuracy and calibration stability of the assembled system with discussion concerning imperfections imposed by real radio environment. Results of measurements are summarized in the last chapter, where conclusions are drawn.

Chapter 2

AoA estimation: state of the art in algorithms and SDR-based implementations

2.1 Algorithms for angle estimation

Extracting information about angle of arrival from signals received at multiple antenna ends has been thoroughly studied resulting in specific approaches and algorithms. On the whole, DoA methods can be divided into 3 groups [23].

1. Beamforming methods - basing on performing a scanning sweep in all possible directions and measuring output power of the array at given angle. Peak in the power corresponds to the direction of arrival. Several enhancements have been proposed to this group, like employing spectral analysis tools, resulting in Bartlett method or Capon beamformer. Even in favorable conditions these methods do not take the full advantage of the information provided in the RX data streams.
2. Subspace methods - utilize geometrical properties of the data model. Employing eigendecomposition of the covariance matrix to extract noise and signal eigenvectors which correspond to sources present in the data. Two most distinguished algorithms of this group are: Multiple SIgnal Classification (MUSIC) and Estimation of Signal Parameters via Rotational Invariant Techniques (ESPRIT). Greater complexity in computation results in superresolution of obtained estimations and ability to separate even closely located sources.
3. Parametric methods - apply statistical framework to data in order to extract an estimator with selected optimality properties. This approach utilizes Maximum Likelihood estimator (ML) and its derivations like Deterministic ML, Stochastic ML or Conditional ML. Most popular of this kind are: space-alternating generalized expectation-maximization (SAGE) and RELAX algorithm.

As reported by simulations in [23] best resolution is achieved by parametric methods basing on maximum likelihood. Closest to the accuracy provided by ML methods is root-MUSIC algorithm. In case of computational complexity the ML methods require multi-dimensional nonlinear optimization, which is associated with N -dimensional search. Taking this into consideration subspace methods offer a compromise solution in terms of computational complexity and accuracy.

2.2 Signal and noise subspaces in the context of uniform linear array

MUltiple SIgnal Classification (MUSIC) algorithm is a subspace-based method of direction estimation. This group of methods in general relies on exploiting the orthogonality between signal and noise subspaces. To provide better understanding of the principles underlying the theory behind the algorithm it is necessary to start with characterisation of signal received by an array. Presume that antenna array consists of N isotropic receivers, which are located at position \mathbf{p}_n expressed as:

$$\mathbf{p}_n = [p_{x_n} \ p_{y_n} \ p_{z_n}] \quad n \in \{0, 1, \dots, N - 1\} \quad (2.1)$$

For uniform linear array with elements distributed alongside Z axis, position of antenna elements in space with array center at $[0, 0, 0]$ can be described as follows:

$$p_{x_n} = 0, \ p_{y_n} = 0, \ p_{z_n} = \left(n - \frac{N-1}{2}\right) d \quad n = 0, 1, \dots, N - 1 \quad (2.2)$$

where d is the spacing between the antennas expressed in meters. Graphical representation of the array construction can be found in Fig. 2.1.

Spatial separation of antennas introduces phase shift between signals received by each element of the array. Phase difference is determined by angle of incidence in regard to array axis and index of the antenna element. In case of a single source the signal received by the array can be described as:

$$\mathbf{x}(t) = \tilde{s}(t)\mathbf{v}(k) + w(t) \quad (2.3)$$

where, $\mathbf{v}(k)$ is the **array manifold vector** (AMV), which defines phase shifts in respect to the reference point of the array depending on argument k characterizing the direction of arrival. White additive noise is designated as $w(t)$. From geometric relationships and analysis of signal path differences from Fig. 2.1 AMV for linear array can be written as:

$$\mathbf{v}(k) = \left[e^{j\left(\frac{N-1}{2}\right)d\frac{2\pi}{\lambda}\cos(\theta)} \ e^{j\left(\frac{N-3}{2}\right)d\frac{2\pi}{\lambda}\cos(\theta)} \ \dots \ e^{-j\left(\frac{N-1}{2}\right)d\frac{2\pi}{\lambda}\cos(\theta)} \right]^T \quad (2.4)$$

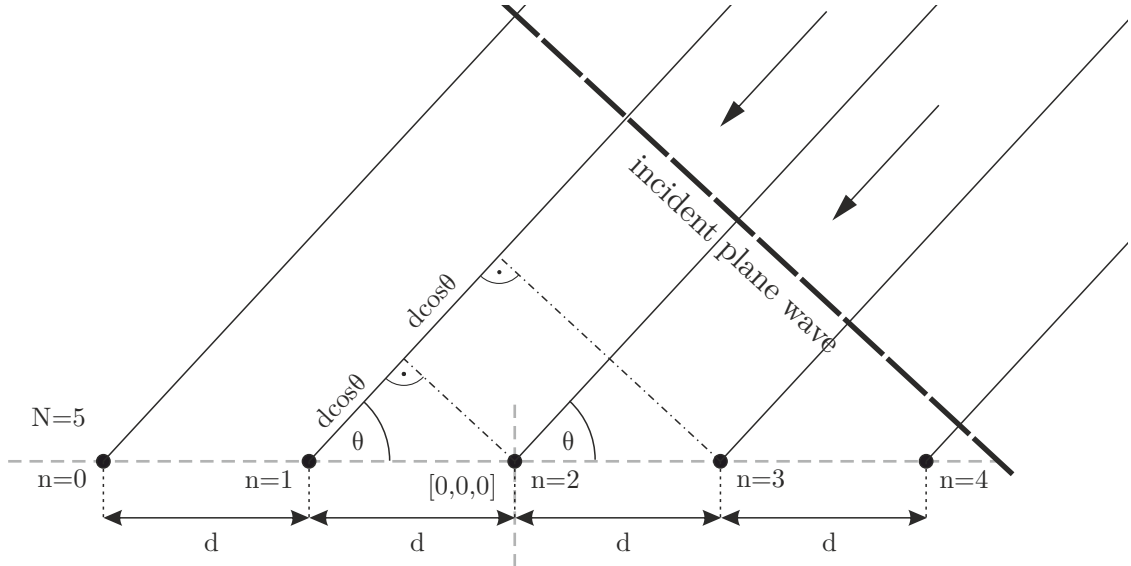


Figure 2.1: Uniform linear array with an incident plane wave.

It can be seen that the signal received by each antenna is multiplied by phase shift coefficient $e^{j\phi}$ consisting of two components $\pm (\frac{N-1}{2})$ – multiplier introduced by position in regard to the center of the array and $\frac{2\pi}{\lambda} \cos(\theta)$ representing phase shift determined by direction of arrival and wavelength of signal.

Angle dependent phase shift for uniform linear array (ULA) distributed along Z axis can be expressed as:

$$k_z = -\frac{2\pi}{\lambda} \cos(\theta) \quad (2.5)$$

where $\frac{2\pi}{\lambda}$ component is referenced as *angular wavenumber*, that describes the phase of the signal depending on the wavelength. Substituting position based shift multiplier with \mathbf{p}_n defined in (2.1) the AMV of the linear array can be further simplified to:

$$\mathbf{v}(\mathbf{k}) = [e^{-jk_z^T \mathbf{p}_0} \ e^{-jk_z^T \mathbf{p}_1} \ \dots \ e^{-jk_z^T \mathbf{p}_{N-1}}]^T \quad (2.6)$$

Formula derived in (2.6) can be modified to represent general case AMV of arbitrary array shapes. In order to achieve this k_z needs to be replaced with \mathbf{k} – *wave vector*, which describes direction of wave propagation in space. It is achieved by employing unit vector \mathbf{u} and calculating angle relations, which characterize the direction in spherical coordinate system. Center of the system corresponds to the central point of the array. Graphical interpretation of the unit vector and relations between axes and angles can be found in Fig. 2.2.

$$\mathbf{k} = -\frac{2\pi}{\lambda} \mathbf{u} = -\frac{2\pi}{\lambda} [\sin(\theta) \cos(\phi) \ \sin(\theta) \sin(\phi) \ \cos(\theta)]^T \quad (2.7)$$

For general case the array manifold vector is defined as follows:

$$\mathbf{v}(\mathbf{k}) = [e^{-jk^T \mathbf{p}_0} \ e^{-jk^T \mathbf{p}_1} \ \dots \ e^{-jk^T \mathbf{p}_{N-1}}]^T \quad (2.8)$$

Similar generalization can be performed for signal received by the array in (2.3) when there are D signal sources generating directional plane-wave processes. It is then formulated as:

$$\mathbf{x}(t) = \sum_{m=1}^D \tilde{s}_m(t) \mathbf{v}(\mathbf{k}_m) + w(t) \quad (2.9)$$

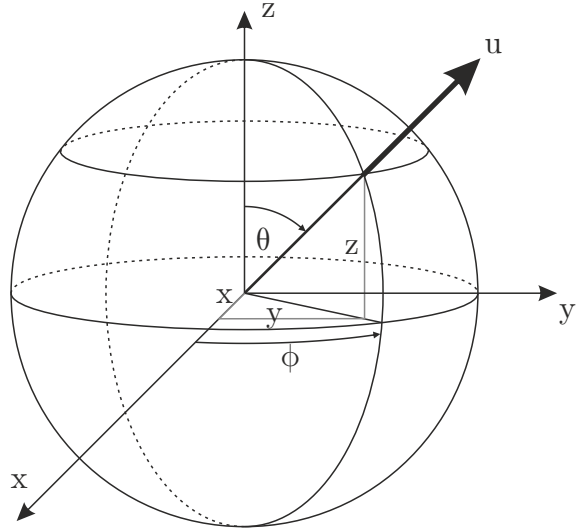


Figure 2.2: Spherical coordinate system and direction vector \mathbf{u} .

Notice that array manifold vector is evaluated for each *wave vector* \mathbf{k}_m representing direction of arrival of signal emitted by m th source – target.

Signal received by the array can be expressed in matrix form as:

$$\mathbf{X} = \mathbf{S}\mathbf{V} + \mathbf{W} \quad (2.10)$$

where,

$$\mathbf{X} := [x_0(t) \ x_1(t) \ \dots \ x_{N-1}(t)]^T \quad (2.11)$$

$$\mathbf{S} := [s_1(t) \ s_2(t) \ \dots \ s_D(t)]^T \quad (2.12)$$

$$\mathbf{V} := [\mathbf{v}(\mathbf{k}_1) \ \mathbf{v}(\mathbf{k}_2) \ \dots \ \mathbf{v}(\mathbf{k}_D)]^T \quad (2.13)$$

$$\mathbf{W} := [w_0(t) \ w_1(t) \ \dots \ w_{N-1}(t)]^T \quad (2.14)$$

\mathbf{X} is a vector of signals received by each element of the array – it is identical to the signal vector presented in (2.9), \mathbf{S} is the sources signal vector, \mathbf{V} is the *array manifold matrix* created from evaluation of AMV for each source wave vector and \mathbf{W} is the white noise vector.

To obtain discrete form of signal suppose that source signals $\tilde{s}_m(t)$ are band limited to B and sampling is performed at rate of $1/B$. Simultaneous sampling across all antenna elements results in discrete-time data snapshot, which is a vector of samples from all N antenna elements. Covariance matrix of the input data can be calculated as:

$$\mathbf{R}_{\mathbf{x}}(k) = E[\mathbf{x}(k)\mathbf{x}^H(k)] \quad \vee \quad \mathbf{R}_x(k) = E[\mathbf{X}(k)\times\mathbf{X}^H(k)] \quad (2.15)$$

where snapshot for each moment in time is denoted as $\mathbf{x}(k) \vee \mathbf{X}(k)$ with $k = 1, 2, \dots, T$.

If both signals and noise are uncorrelated, the sensor covariance matrix for specified moment in time can be represented as:

$$\begin{aligned} \mathbf{R}_{\mathbf{x}} &= E[\mathbf{X} \times \mathbf{X}^H] \\ &= E[(\mathbf{S}\mathbf{V} + \mathbf{W}) \times (\mathbf{S}\mathbf{V} + \mathbf{W})^H] \\ &= \mathbf{V}E[\mathbf{S}\mathbf{S}^H]\mathbf{V}^H + E[\mathbf{W}\mathbf{W}^H] \\ &= \mathbf{V}\mathbf{R}_{\mathbf{s}}\mathbf{V}^H + \sigma_w^2 \mathbf{I} \end{aligned} \quad (2.16)$$

From above derivation it can be seen that sensor covariance matrix has two components, the first one is signal covariance matrix and the other being noise covariance matrix. $\mathbf{R}_{\mathbf{s}}$ is a source covariance matrix, which diagonal elements represent source powers and off-diagonal express source correlations. MUSIC algorithm assumes uncorrelated sources and noise with equal power across all receiving elements. As a result second component of covariance matrix – the noise covariance matrix is a diagonal matrix with equal values of noise power σ_w^2 along the diagonal.

True array covariance matrix $\mathbf{R}_{\mathbf{x}}$ can be estimated using different approaches, which influence the accuracy of AoA algorithms. One method is to estimate the matrix from an average of multiple data snapshots. Calculated estimation matrix is referenced as $\mathbf{C}_{\mathbf{x}}$ – the sample correlation matrix. Size of the covariance and correlation matrix is determined by number of antenna elements and is equal to $[N \times N]$.

$$\mathbf{C}_{\mathbf{x}} = \frac{1}{T} \sum_{k=1}^T \mathbf{x}(t_k) \mathbf{x}^H(t_k). \quad (2.17)$$

Equivalent method is based on gathering K sample snapshots which are formed into matrix marked as \mathbf{X}_K of size $[N \times K]$. The sample correlation matrix is a result of operation:

$$\mathbf{C}_x = \frac{1}{K} \mathbf{X}_K \mathbf{X}_K^H \quad (2.18)$$

Improved DoA performance can be achieved with Foward-Backward averaging of the sample correlation matrix, which is widely described in [26]. It is applicable to symmetrical array geometries, so that AMV is conjugate symmetric. Use of reflection matrix \mathbf{J} , which is square of size $[N \times N]$ with cross diagonal elements being unity and others equal to 0, introduces a centrohermitian constraint that maximizes the likelihood of \mathbf{R}_x estimate. This method of averaging is reported to return results of superior accuracy with MUSIC algorithm. Forward-backward averaging of sample correlation matrix is expressed as:

$$\mathbf{C}_x = \frac{1}{2K} \mathbf{X}_K \mathbf{X}_K^H + \frac{1}{2K} \mathbf{J} \mathbf{X}_K^* \mathbf{X}_K^T \mathbf{J} \quad (2.19)$$

Substituting the true sensor covariance matrix with an estimate results in:

$$\mathbf{C}_x = \mathbf{V} \mathbf{R}_s \mathbf{V}^H + \sigma_w^2 \mathbf{I} \quad (2.20)$$

Key assumption of subspace methods is that no signal sources or noise are correlated. This constraint determines that \mathbf{R}_s is positive definite Hermitian matrix with full rank D . Consequently $\mathbf{V} \mathbf{R}_s \mathbf{V}^H$ also has rank D , ($D < N$) guaranteeing D positive real eigenvalues and $N - D$ zero eigenvalues.

Eigenvalue decomposition (EVD) of square Hermitian matrix \mathbf{A} is derived as follows:

$$\mathbf{A} \Phi = \lambda \Phi \quad (2.21)$$

where λ is a scalar value referenced as eigenvalue of \mathbf{A} and Φ represents eigenvectors of \mathbf{A} that satisfy the equation. The relation can be written as:

$$[\lambda \mathbf{I} - \mathbf{A}] \Phi = 0 \quad (2.22)$$

Roots of the equation below are eigenvalues of \mathbf{A} :

$$\det(\lambda \mathbf{I} - \mathbf{A}) = 0 \quad (2.23)$$

Each eigenvalue has at least one eigenvector associated to it. Eigenvectors of unequal eigenvalues are linearly independent – orthogonal to one another. To calculate the eigenvector, determined eigenvalue is substituted to (2.22) and resultant equation is solved for Φ .

The columns of array manifold matrix \mathbf{V} define a D -dimensional subspace containing all the signal energy. Orthogonal basis for this subspace is provided by eigenvectors. Therefore, each eigenvector designated as Φ_d for each of the d sources from range of $d = 1, 2, \dots, D$ can be obtained from \mathbf{V} by performing linear transformation represented by vector \mathbf{c}_d of shape $[D \times 1]$:

$$\Phi_d = \mathbf{V} \mathbf{c}_d \quad (2.24)$$

Eigendecomposition equation of the first component from (2.20) is:

$$\lambda \Phi_d = \mathbf{V} \mathbf{R}_s \mathbf{V}^H \Phi_d \quad (2.25)$$

Then representing the eigenvector as linear transformation yields:

$$\lambda \mathbf{V} \mathbf{c}_d = \mathbf{V} \mathbf{R}_s \mathbf{V}^H \mathbf{V} \mathbf{c}_d \quad (2.26)$$

Equation can be rewritten as:

$$\mathbf{V} [\lambda \mathbf{I} - \mathbf{R}_s \mathbf{V}^H \mathbf{V}] \mathbf{c}_d = \mathbf{0} \quad (2.27)$$

Above equation can be satisfied with D solutions ($\lambda_1^s \geq \lambda_2^s \geq \dots \geq \lambda_D^s$), which are eigenvalues associated with the signal component of \mathbf{X} .

$$\det [\lambda \mathbf{I} - \mathbf{R}_s \mathbf{V}^H \mathbf{V}] = 0 \quad (2.28)$$

Associated with each signal subspace eigenvalue is eigenvector marked as Φ_d that can be obtained from \mathbf{c}_d by solving (2.27) for each \mathbf{c}_d and then evaluating (2.24) to obtain Φ_d . Products of this operation formed into $[N \times D]$ matrix are considered the signal subspace formulated as:

$$\mathbf{U}_S := [\Phi_1 \quad \Phi_2 \quad \dots \quad \Phi_D] \quad (2.29)$$

On the contrary, the latter – noise component of covariance matrix in (2.20) spans the entire N-dimensional subspace. To represent it $N - D$ additional orthogonal vectors are required. Any vectors that are orthogonal to each other and the signal subspace \mathbf{U}_S meet the criteria. Corresponding eigenvalue to selected vectors is σ_w^2 . From calculated eigenvectors matrix of size $[N \times (N - D)]$ is assembled and referenced as \mathbf{U}_N the noise subspace.

$$\mathbf{U}_N := [\Phi_{D+1} \quad \Phi_{D+2} \quad \dots \quad \Phi_N] \quad (2.30)$$

On the whole, sample correlation matrix can be expressed with eigenvalues and eigenvectors calculated throughout the decomposition.

$$\mathbf{C}_x = \sum_{i=1}^N \lambda_i \Phi_i \Phi_i^H \quad (2.31)$$

where,

$$\lambda_i = \begin{cases} \lambda_i^s + \sigma_w^2, & \text{if } i = 1, 2, \dots, D \\ \sigma_w^2, & \text{if } i = D + 1, D + 2, \dots, N \end{cases} \quad (2.32)$$

Alternatively, correlation matrix may be represented as a sum of signal and noise subspace, with the use of $[D \times D]$ diagonal matrix with eigenvalues along the main diagonal, designated as $\Lambda_S := \text{diag}[\lambda_1, \lambda_2, \dots, \lambda_D]$ and the $[(N - D) \times (N - D)]$ diagonal matrix $\Lambda_N = \sigma_w^2 \mathbf{I}$:

$$\mathbf{C}_x = \mathbf{U}_S \Lambda_S \mathbf{U}_S^H + \mathbf{U}_N \Lambda_N \mathbf{U}_N^H \quad (2.33)$$

Separation of signal subspace from noise subspace and utilization of their orthogonality is a central element of MUSIC angle of arrival estimation algorithm.

2.3 Multiple Signal Classification based method of direction of arrival estimation

Requirements and constraints

Before attempting to present the MUSIC algorithm it is essential to mention its requirements and limitations:

- Detected waveform should be narrow-band and signal sources should be uncorrelated.
- Received noise needs to be uncorrelated and of equal power between antennas.

- Arriving signals should be in a form of a plane wave – far field working regime.
- Number of antenna elements has to be greater than number of signals to be detected. If D is the number of signals, at least $D + 1$ antenna elements are required.
- Number of signals, which AoA is to be estimated needs to be known beforehand.
- Physical dimensions of antenna array should be considerably smaller than distance from the target source.
- Signal processing performed in the front end and sampling of data is perfectly synchronized in regard to frequency, time and phase.

MUSIC algorithm

MUSIC algorithm for angle of arrival estimation with use of uniform linear array can be described with psuedocode as follows:

Algorithm MUSIC

- 1: Calculate sample correlation matrix \mathbf{C}_x using method presented in (2.18) or (2.19).
 - 2: Determine the \mathbf{U}_N – the noise subspace by performing EVD on \mathbf{C}_x and selecting eigenvectors corresponding to the smallest ($N - D$) eigenvalues.
 - 3: **for** Angle range of interest: $0 \leq \phi \leq \pi$ **do**
 - 4: Generate the array manifold vector for each angle, $\mathbf{v}(\phi)$, in accordance to (2.6).
 - 5: Compute the *pseudospectrum* as:
- $$P(\phi) := \frac{1}{\|\mathbf{v}^H(\phi)\mathbf{U}_N\|^2} = \frac{1}{\mathbf{v}^H(\phi)\mathbf{U}_N\mathbf{U}_N^H\mathbf{v}(\phi)}.$$
- 6: Choose the D maximas of $P(\phi)$. The corresponding values of ϕ are the D angles of arrival.
-

When evaluated angle ϕ is equal to the true direction of arrival, $\mathbf{v}(\phi)$ will be a vector from signal basis, which is orthogonal to the noise subspace. Result of multiplication of these two components should be equal to zero. Due to inaccuracies of estimation and presence of the noise vectors will not be truly orthogonal and result will be of negligible value. Low values in the denominator create a peak in the *pseudospectrum* corresponding to the true angle of arrival.

Instead of calculating MUSIC algorithm *spectrum* as defined above it is possible to omit number reciprocity operation. It is then referred as the *null-spectrum* represented by:

$$Q(\phi) := \|\mathbf{v}^H(\phi)\mathbf{U}_N\|^2 = \mathbf{v}^H(\phi)\mathbf{U}_N\mathbf{U}_N^H\mathbf{v}(\phi) \quad (2.34)$$

In this form angles of arrival correspond to the minima in the *null-spectrum* plot.

Root MUSIC algorithm

Root MUSIC algorithm focuses on finding roots of polynomial representation of the *null-spectrum* instead of performing a search for peaks in *pseudospectrum* sampled at potential arrival angles. In order to represent the *null-spectrum* in polynomial form it is necessary to differently express *array manifold vector* defined in (2.4) for linear array. By excluding the common part of the phase shift coefficient $e^{-j(\frac{N-1}{2})\psi}$ before the vector and defining $\psi = -k_z d$, the AMV vector of ULA can be rewritten as:

$$\mathbf{v}(\psi) = e^{-j(\frac{N-1}{2})\psi} \begin{bmatrix} 1 & e^{j\psi} & \dots & e^{j(N-1)\psi} \end{bmatrix}^T. \quad (2.35)$$

Phase shifting the obtained vector by $e^{j(\frac{N-1}{2})\psi}$ and performing substitution: $e^{j\psi} = z$, representation of the vector can be simplified to:

$$\tilde{\mathbf{v}}(z) = [1 \ z \ \dots \ z^{N-1}]^T. \quad (2.36)$$

With the phase shift expressed by $\{z\}$ formula for *null-spectrum* takes form of:

$$Q(z) = \tilde{\mathbf{v}}^T(1/z)\mathbf{U}_N\mathbf{U}_N^H\tilde{\mathbf{v}}(z) \quad (2.37)$$

Notice that, the phase shifted version of the *array manifold vector* does not influence spectrum magnitude due to the fact that modulus of the original AMV remains unchanged.

Next, the *square* of \mathbf{U}_N is defined as:

$$\mathbf{U}_N^2 := \mathbf{U}_N\mathbf{U}_N^H \quad (2.38)$$

To further simplify the notation , shift introduced by modified AMV is expressed as $z^{\pm n}$ with the notion, that $z = e^{j\psi}$,

$$Q(z) = \sum_{m=0}^{N-1} \sum_{n=0}^{N-1} z^{-m} \mathbf{U}_N^2(m, n) z^n \quad (2.39)$$

Above expression can be rephrased to form of:

$$Q(z) = \sum_{l=-N+1}^{N-1} c_l z^l. \quad (2.40)$$

Where $\{c_l\}$ is a sum of elements along selected diagonal, for $l > 0$ it is in regard to l th super-diagonal and if $l < 0$ it applies to l th sub-diagonal. As has been previously noted \mathbf{U}_N^2 is a Hermitian non-negative definite matrix, so that $c_l = c_{-l}^*$. Because of this symmetry only $N - 1$ polynomial coefficients need to be calculated to find roots of this equation.

In the ideal case roots of normalized *null-spectrum* polynomial would lie on the unit circle due to applied normalization. Unit circle is regarded as set of complex numbers of constant magnitude equal to unity. Values of the numbers are represented by a circle on complex plane centered at origin with radius of one. However, due to noise and other imperfections D roots will not necessarily lay on unit circle. Therefore, for further processing roots that are inside of the unit circle and closest to it are selected. This is achieved by selecting roots which magnitude is smaller than one, but closest to the unity.

Algorithm Root MUSIC

- 1: Calculate sample correlation matrix \mathbf{C}_x using method presented in (2.18) or (2.19).
 - 2: Determine the \mathbf{U}_N – the noise subspace by performing EVD on \mathbf{C}_x and selecting eigenvectors corresponding to the smallest $(N - D)$ eigenvalues.
 - 3: Calculate \mathbf{U}_N^2 – the *square* of noise subspace according to (2.38).
 - 4: Determine the $Q(z)$ – *null-spectrum* polynomial coefficient vector according to (2.40) and normalize it.
 - 5: Determine roots of $Q(z)$, by assigning the polynomial vector to last column of Frobenius companion matrix and performing EVD on it. Obtained eigenvalues are roots of the $Q(z)$.
 - 6: Choose D roots, $\{z_i\}$ for $i = 1, 2, \dots, D$, which are inside the unit circle and closest to it.
 - 7: Calculate the angle of arrival from selected roots $\{\theta_i\}$ for $d = 1, 2, \dots, D$ using the formula:

$$\theta_i = \text{acos}\left(\frac{\lambda}{2\pi d} \arg(z_i)\right).$$
-

Root MUSIC algorithm returns results independent of the quantization of angle range for which values of *pseudo* or *null-spectrum* are calculated. It also requires less operations resulting in lower computational complexity. Due to straight forward approach to calculate the roots, that

correspond to angles, greater precision is achieved. MUSIC algorithm can be generalized for arbitrary geometries including planar or 3D arrays. In case of Root MUSIC algorithm different array geometry involves derivation of applicable formulas.

2.4 Synchronization and calibration

Main component determining overall accuracy of the AoA estimation is synchronization of antenna array elements. There are 3 domains in which the signal sampling and processing needs to be aligned to provide reliable data for further analysis:

Frequency – every receiving radio front end needs to share the same reference clock providing signal of certain frequency to the RF front end and DSP section. Even the smallest difference in frequencies will cause a fluctuating phase shift between signals that will distort angle estimation.

Consider a pass-band signal $x(t)$, which is received by two RF front ends, for simplicity no phase difference caused by different propagation distance is considered.

$$x(t) = s(t)e^{j2\pi f_c t}. \quad (2.41)$$

One local oscillator of receiver uses the same carrier frequency generating signal $x_{LO1}(t) = e^{-j2\pi f_c t}$. At the same time another frontend has local oscillator generating signal with carrier frequency shifted by f_Δ , i.e., $x_{LO2}(t) = e^{-j2\pi(f_c + f_\Delta)t}$.

Then the down conversion is performed by mixing received signal with the reference local oscillator signal. The result is:

$$x(t)x_{LO1}(t) = s(t)e^{j2\pi f_c t}e^{-j2\pi f_c t} = s(t) \quad (2.42)$$

$$x(t)x_{LO2}(t) = s(t)e^{j2\pi f_c t}e^{-j2\pi(f_c + f_\Delta)t} = s(t)e^{-j2\pi f_\Delta t} \quad (2.43)$$

From simplified calculations it can be seen that when the frequency of the radio front ends is not perfectly matched, additional phase rotation is introduced. This error will change in time.

Phase – antenna array has to be phase coherent as angle of arrival is determined by differences in the phase of received signals.

Similarly to analysis performed for frequency, consider signal $x(t)$ which is received by two RF front ends. Frontends share the same carrier frequency, but the second has some phase offset to the first one φ_Δ .

$$x(t) = s(t)e^{j2\pi f_c t} \quad x_{LO1}(t) = e^{-j2\pi f_c t} \quad x_{LO2}(t) = e^{-j(2\pi f_c t + \varphi_\Delta)} \quad (2.44)$$

Then the down conversion is performed using defined signals:

$$x(t)x_{LO1}(t) = s(t)e^{j2\pi f_c t}e^{-j2\pi f_c t} = s(t) \quad (2.45)$$

$$x(t)x_{LO2}(t) = s(t)e^{j2\pi f_c t}e^{-j(2\pi f_c t + \varphi_\Delta)} = s(t)e^{-j\varphi_\Delta} \quad (2.46)$$

The analysis shows, that phase offset present between local oscillators of the devices is transferred to the demodulated signals. Introduced constant phase offset needs to be compensated to obtain synchronized signals. This may be achieved by multiplying the signal with a complex coefficient in a processing software. Phase of LO in the RF front end remains unchanged but outputted samples appear to be phase aligned due to performed post processing.

Time – every action performed by the devices serving as front ends in the phased array should be performed at the exact same moment in time. This applies to sampling, issuing bit streams and performing operations in DSP. This is mostly accomplished by a Pulse Per Second (PPS) signal that is distributed among devices and serves as gating pulse that resets timers.

Methods of synchronization in those 3 domains are dependent on hardware architecture of devices and vary with each product series or families.

2.5 Literature review

Popularity of Software-defined radio platforms (SDR) in regard to system prototyping and algorithm evaluation has brought about numerous papers concerning implementation of direction of arrival estimation capable systems. Testing the DoA algorithm with hardware requires proper synchronization of channel and devices. It may be troublesome in some SDR architectures with integrated local oscillators and clocks.

Universal Software Radio Peripheral (USRP) devices manufactured by Ettus Research, a National Instruments brand, are especially popular among academic society and widely utilized in experimental setups. Depending on the version of the product its channels may be synchronized by default or require an additional calibration routine. Phase calibration of the radio front ends appears to be a common issue. Due to differences in signal path lengths and tolerance of components constant phase shift between different channels is inevitable. Ettus Research has published a white paper addressing this issue, which describes device synchronization and showcases DoA estimation with the use of X310 device in [6]. Presented one-time calibration routine consists of attaching a signal source via splitter to all RX channel simultaneously. Wiring of receiving ports is depicted in Fig. 2.3. Then, for a short period of time correcting coefficients in a form of phase shift value required to synchronize the array are measured, averaged and saved to file. After the calibration routine wired signal source is replaced with antennas that form the array. Saved phase coefficients compensate phase differences by multiplying the signal with complex value representing the required shift. With this paper comes a GNU Radio package `gr-doa` with signal processing blocks performing AoA estimation, and serving as a fine starting point for evaluation of the algorithm.

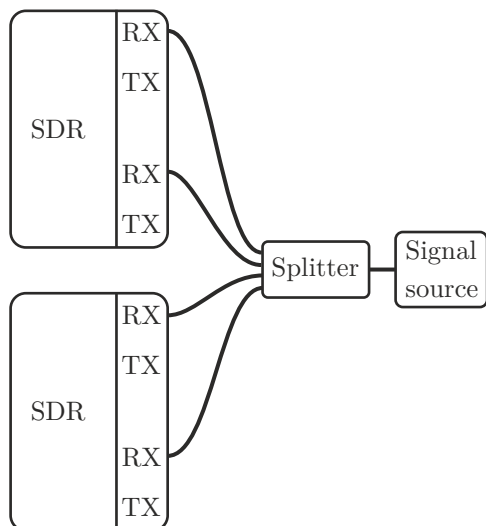


Figure 2.3: Calibration via RX port.

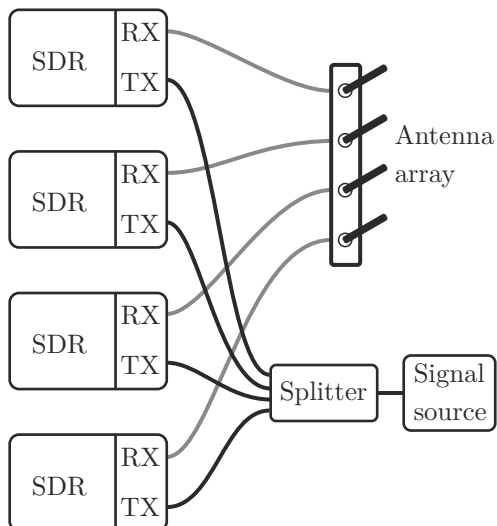


Figure 2.4: Calibration via TX port.

Above mentioned white paper was more widely discussed in a presentation at annual GNU Radio conference [25], where different hardware implementations were described. During the talk, setup consisting of multiple N210 (1 RX + 1 TX) was presented with an unusual calibration method. The phase synchronizing tone was inserted into TX port of the device with matched cable lengths. Due to cross-talk the tone was receivable at the RX side, without the need to connect anything to RX port or rearrange the wiring. Similar TX signal paths introduce repeatable phase shift across the devices providing sufficient calibration accuracy. It should be noted that USRP N210 device clock produces phase ambiguity, which results in random phase offset between channels after each power-up or change of parameters. In USRP B210 phase ambiguity is not present.

It is also possible to visually align signal waveforms in interactive software environment by adjusting the phase shift values. With the reference signal connected to all RX ports via splitter it may help to notice amplitude differences. Such approach was presented in [15]. Whereas it might not be the most accurate method it may be valid for quick evaluation of phases and amplitudes of received signals.

So far presented methods of phase alignment employed coaxial cables to deliver reference signal. Alternative to wired setup is calibration through wireless channel with the use of antennas. Calibration signal is a tone of specified frequency. When antennas are spaced by distance $\{d\}$ received signal phase will differ in regard to reference element. Phase shift introduced by traversing additional distance by waveform can be calculated as:

$$\Delta\varphi = e^{j2\pi \frac{d}{\lambda}} \quad (2.47)$$

where, $\frac{d}{\lambda}$ is referred as *normalized spacing* of antenna elements. Phases of received signals across antenna elements are compared and accordingly to position of each element required phase shifts for syntonization are calculated. Graphical representation of wireless calibration of uniform linear array is shown in Fig. 2.5. Similar single tone phase calibration of front ends was described in [19].

In some cases when the array is required to estimate angle of arrival of a wideband transmission, that cannot be disturbed by any additional calibration tone, phase calibration becomes problematic. Phase offset between channels of SDRs based on Analog Devices front end chips is

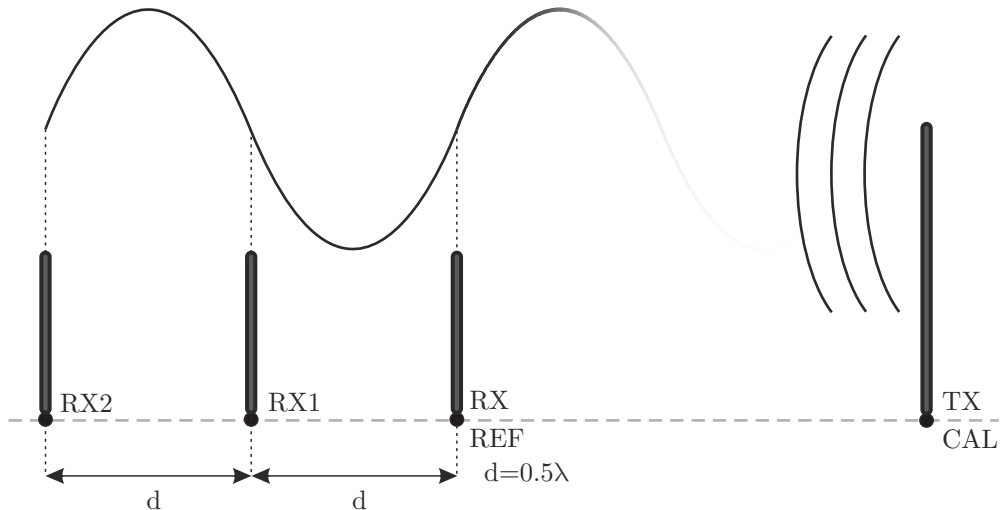


Figure 2.5: Wireless uniform linear array phase calibration method.

proven to exhibit a linear relationship with frequency as presented in [11]. Transmitting a single tone outside of the wideband signal frequency range may provide insufficient phase accuracy. To accurately calibrate phase of the array for center frequency of the wideband signal two pilot tones surrounding the frequency of interest are applied. In the receiver each of the two calibration signals is band pass filtered separately to exclude interference from the wideband signal and the other pilot tone. Then, for each signal respectively required phase shift is calculated. After that, calculated phase shifts obtained from two tones are averaged, resulting in phase shift for center frequency of the wideband transmission, without causing any interference to it. Such approach was presented in [14] and applied to AoA estimation of cellular network signals.

Thermal effects associated with heat up of SDR devices and changing of environmental conditions may introduce drifts or fluctuations of phase shift coefficient. The issue is more widely addressed in [16]. In this work phase drift introduced by hardware heat up is measured over time. Delay from calibration routine is shown to introduce phase error that increases with time and affects estimated AoA. Moreover, measured angle variance is demonstrated to increase in proximity to boundary angles for uniform linear array.

After initial phase and magnitude corrections it may appear, that the AoA algorithms do not yield results of expected accuracy. In this case additional calibration with sources of known angle of arrival and utilizing subspace properties can be applied. Such method is described in [22] with exemplary implementation in publicly available **gr-doa** package.

Chapter 3

Implementation

3.1 Algorithm simulation

In order to obtain reference results and analyze MUSIC algorithm properties series of simulations were performed. Simulation implementation was based on [8] with some additional modifications. Analysis script was implemented in Python language with utilization of NumPy and Matplotlib packages. Prototyping and plotting was additionally accelerated by usage of interactive Jupyter Notebook.

Simulation consisted of following steps:

1. Based on provided number of antenna elements and spacing, ULA position vector is created.
2. Angle vector of specified length is generated with evenly spaced values over range of $[0-\pi]$.
3. Array manifold vector is calculated for each value in angle vector based on generated locations vector and normalized spacing.
4. Signal matrix of defined parameters is created as follows:
 - i. Signal from each source is generated as vector of random sequence of normalized complex samples. Length of generated vector corresponds to set snapshot length (averaging length). Additionally amplitude of the signal can be multiplied to represent different source powers.
 - ii. The signal vector is replicated for each antenna forming temporary array signal matrix for specified source.
 - iii. Generated temporary array signal matrix corresponding to single source is multiplied by array manifold vector calculated for specified angle of arrival.
- a) After every source signal matrix was generated all of matrices are added up.
- b) Finally, matrix of white noise of power calculated from provided SNR is generated and added to the signal matrix.
5. Correlation matrix is calculated from generated array signal matrix using formula (2.18).
6. MUSIC algorithm described in section 2.3 is employed to process generated correlation matrix.
7. Returned pseudospectrum vector is plotted or search for peaks, corresponding to angles of arrival, is performed.

Initially, a singular run of MUSIC algorithm was executed in order to investigate generated pseudospectrum plot and obtain reference result which are visible in Fig. 3.1. Simulation was run with following parameters: 2 sources of equal power located at angles of 50° and 120° , 4 receiving elements with spacing of 0.5λ , snapshot length of 1024 samples, pseudospectrum vector length of 1800 for angle values in range from 0 to π , SNR equal to 10 dB. To evaluate how the pseudospectrum plot is affected by a change in parameters a series of simulation runs were performed with a sweep of most crucial variables. In each analysis most of the parameters remain as in reference simulation, only the ones addressed in description are changed.

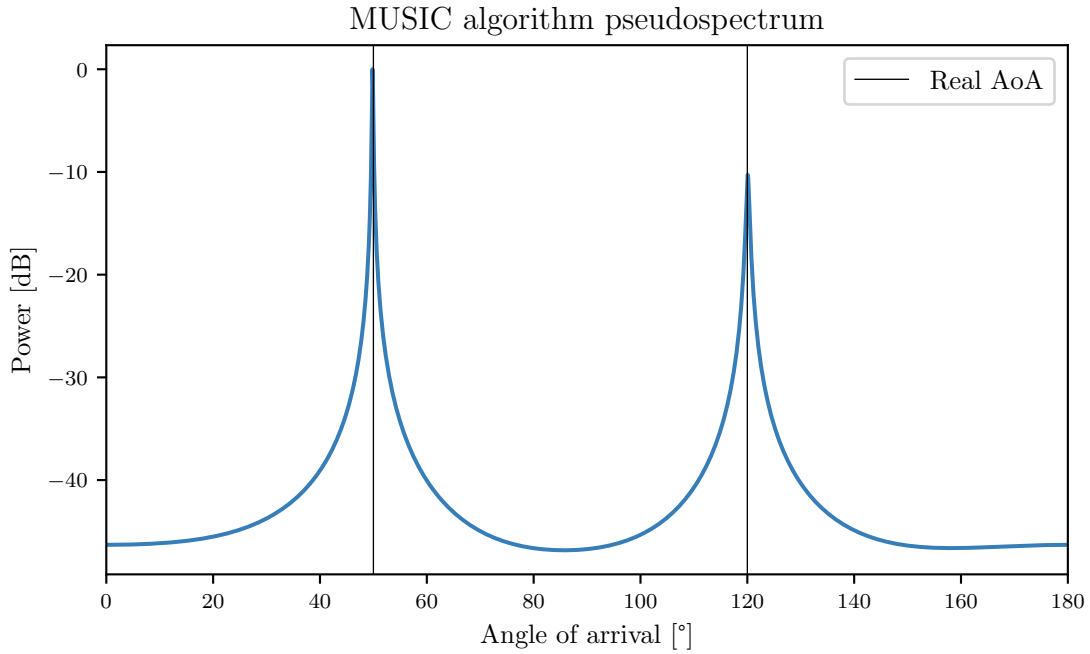


Figure 3.1: Reference MUSIC pseudospectrum plot.

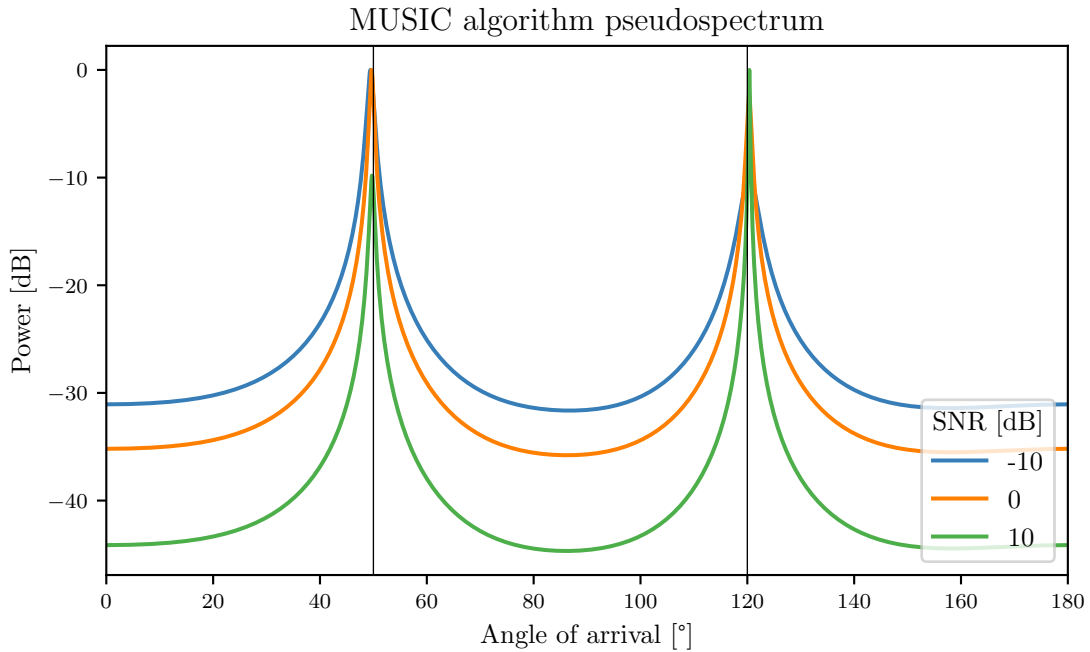


Figure 3.2: Music algorithm pseudospectrum in regard to changes in SNR.

First analysis was performed for three SNR levels: $-10, 0, 10$ [dB]. As can bee noticed in Fig. 3.2, which is a result of single algorithm run for each SNR value, MUSIC algorithm provides reliable results even when signal is dominated by noise. What is more, the pseudospectrum noise level – determined as the lowest point in the plot, decreases with the the increase of SNR levels.

To more precisely portray the relationship between SNR and accuracy of estimation statistical analysis was performed. For the same array parameters and single source positioned at 50° SNR was changed from -15 to 30 dB. For each SNR value simulation was repeated 500 times and estimated AoA was saved. Each time signal and noise sample values were calculated again. To increase accuracy pseudospectrum vector length was extended to 18000 resulting in angle quantization of 0.01° . Results of the analysis are presented in Fig. 3.3. Plotted relationship shows how increase in SNR results in enhancement of estimation accuracy. The slope of the function determines how advantageous is increase in power transmitted by source in exchange for greater accuracy at constant noise levels.

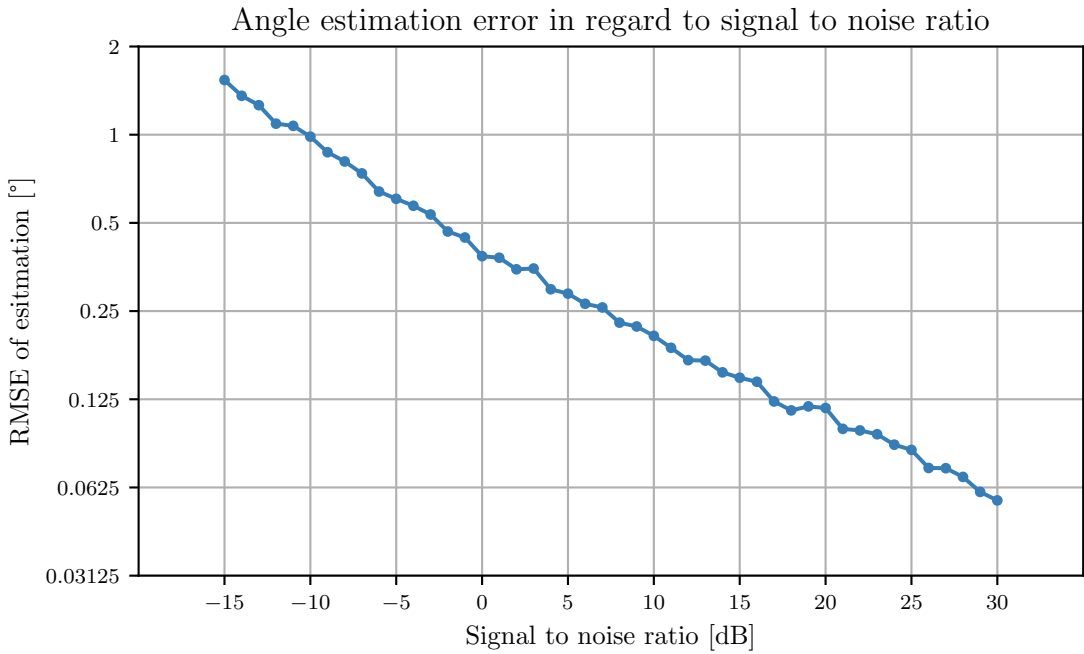


Figure 3.3: RMSE of angle estimation in regard to SNR.

Next simulation focused on how the number of receiving elements affects algorithm pseudospectrum. Antenna count was changed in three steps: 4, 8, 16. For each value a singular MUSIC simulation was executed. Increase in the number of receiving elements resulted in narrowing of the signal peaks and flattening of the noise level as can be noticed in Fig. 3.4. For greater number of sensors the pseudospectrum no longer has characteristic low order polynomial curvature. According to theory the algorithm is capable of determining $(N - 1)$ signal sources. Along with addition of antenna elements the pseudospectrum plot is flattened and resembles a polynomial of higher order which can contain more peaks corresponding to signal sources.

Another significant parameter is the length of snapshot used in calculation of the correlation matrix. In this case snapshot length is equal to averaging length and the terms be used interchangeably. It determines the refresh rate of the pseudospectrum plot as well as rate at which the results are returned at given sample rate. It should be noted that properties of the wireless channel and transmitted signals or symbols rapidly change. Selecting the right value depends on

properties of observed signal, required estimation accuracy, allowed time lag and computational load.

As can be noticed in Fig. 3.5, relatively low snapshot length introduces inaccuracy, which is caused by insufficiently averaged correlation matrix. Peaks visible in the pseudospectrum are smoothed and shifted sideways due to an error. To more clearly portray the relation between the angle estimation error and snapshot length, additional simulation was performed.

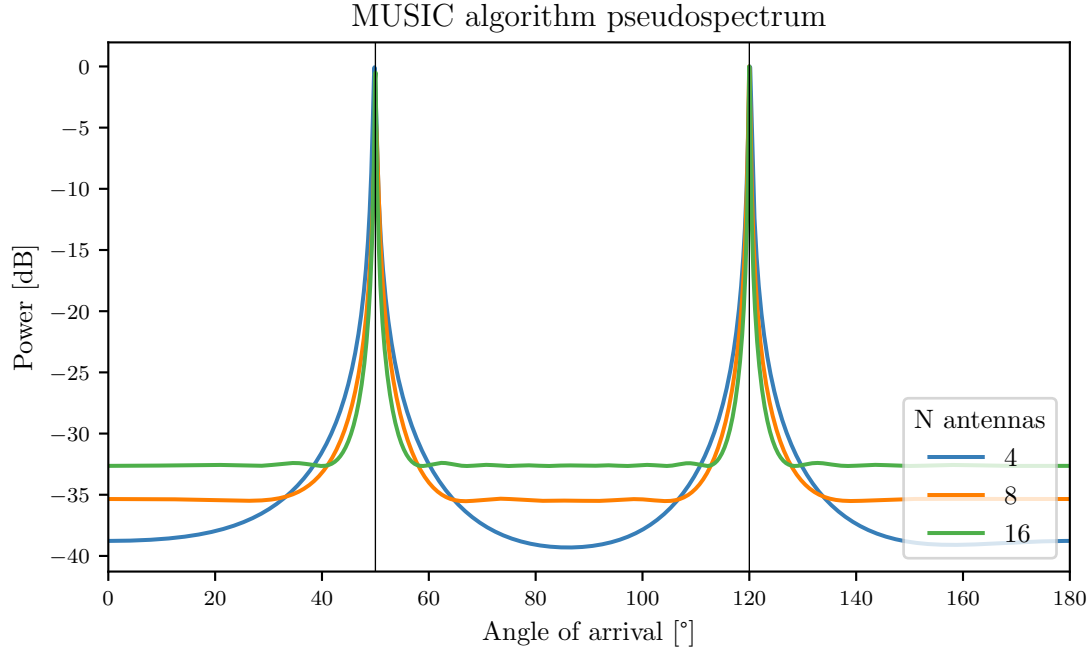


Figure 3.4: Music algorithm pseudospectrum in regard to change in number of antenna elements.

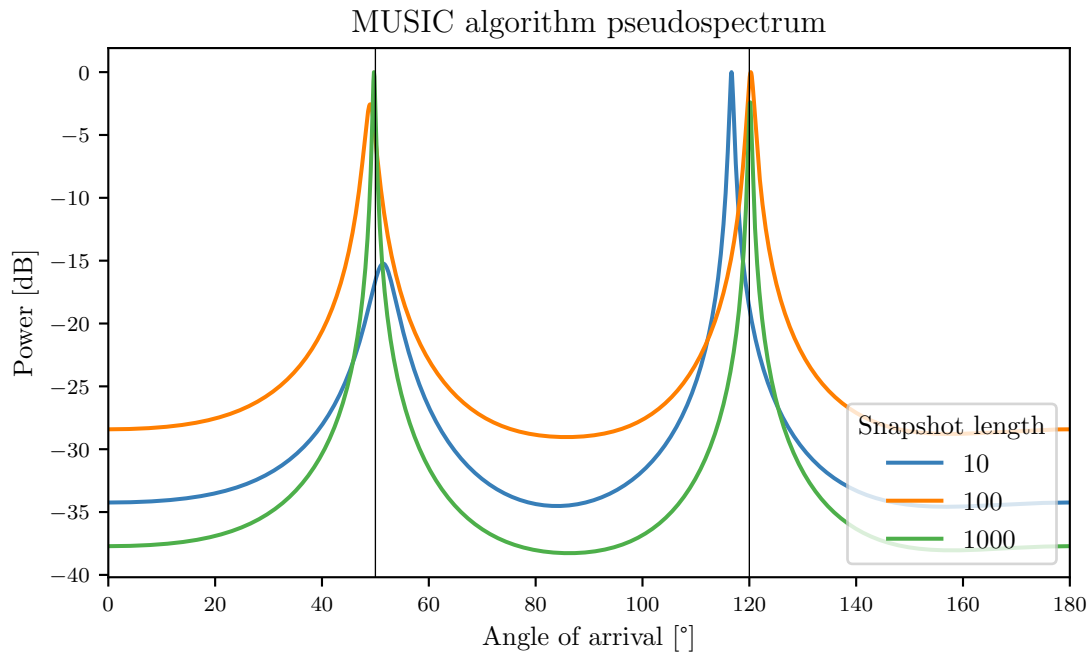


Figure 3.5: Music algorithm pseudospectrum in regard to change in snapshot length.

For each 50 snapshot sizes ranging from 4 to 1024, 500 runs of simulation were executed. Configuration was similar to previous case used to generate Fig. 3.3, apart from pseudospectrum length which was set to 1800. From the results presented in Fig. 3.6 it is clearly visible, that greater number of snapshots used to calculate single correlation matrix provides better accuracy. The RMSE decreases proportionally to logarithm of snapshot length.

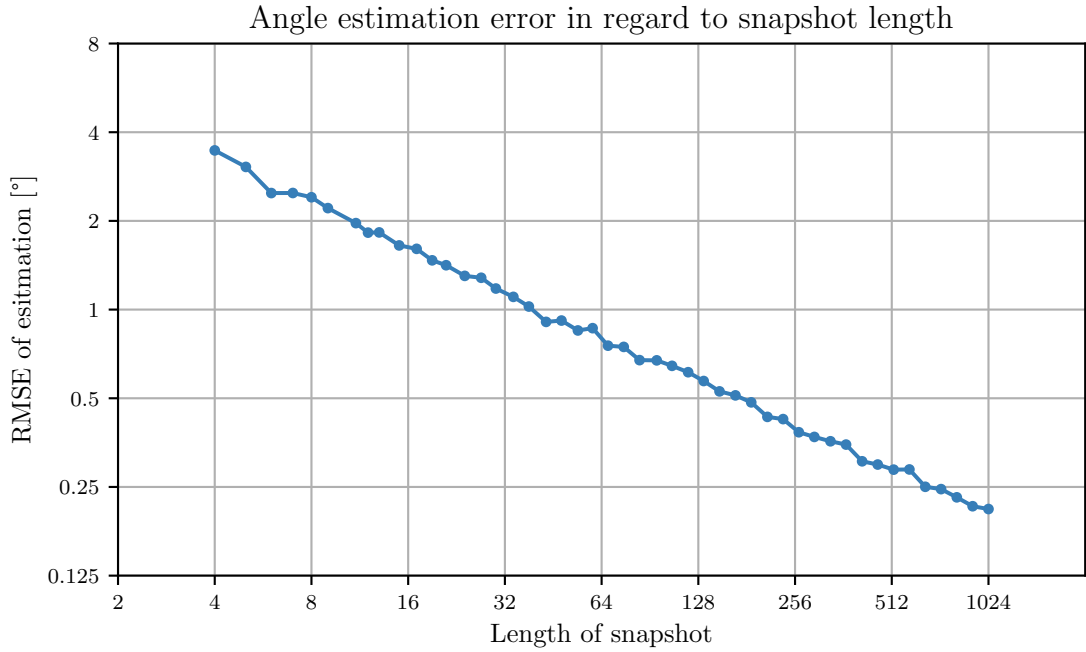


Figure 3.6: RMSE of angle estimation in regard to snapshot length.

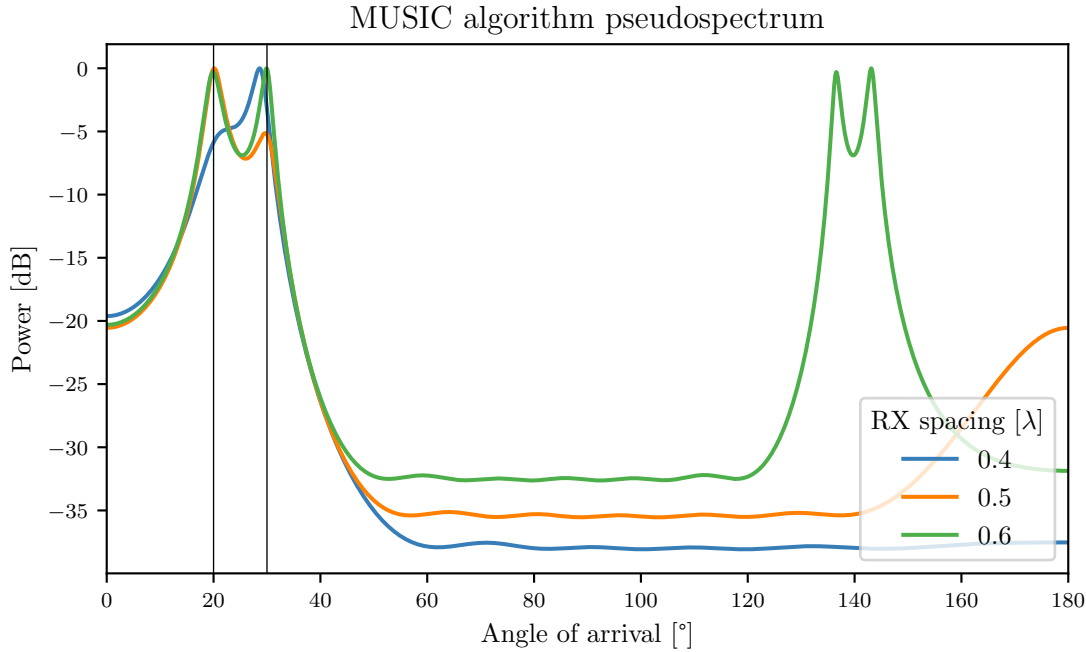


Figure 3.7: MUSIC algorithm pseudospectrum in regard to change in spacing of antenna elements.

Next, simulation focused on investigating how antenna spacing influences the shape of spectrum and results returned by MUSIC algorithm. Pseudospectrum was plotted for three values: 0.4, reference of 0.5 and 0.6 λ . Number of antenna elements was increased to 8 and source angles were changed to 20 and 30°. For each value of antenna spacing array manifold vector was recalculated, so that signals matrices and MUSIC algorithm were evaluated for properly defined parameters.

Influence of element spacing on MUSIC pseudospectrum can be seen in Fig. 3.7. For values below half wavelength, plot is smoothed with peaks shifted by an error in estimation but approximately close to the real angles. Spacing greater than half wavelength introduces significant error in the form of mirrored peaks, due to received signal phase ambiguities. Spacing of 0.5 λ is considered optimal for uniform linear phased arrays as it provides that signal arriving at adjacent antenna elements can be shifted at most by 180°, and room for phase ambiguities is reduced.

More detailed dependency can be found in Fig. 3.8, where another Monte-Carlo simulation was executed. For a set of antenna spacings from 0.01 to 0.5 λ , simulation was repeated till 500 AoA values were gathered. Due to the fact that for antenna spacing greater than 0.5 λ mirror peaks appear in pseudospectrum, which can be seen in Fig. 3.7, analysis was limited to 0.5 λ . For spacing over 0.5 λ presence of false peaks introduces an error dependent of their position in pseudospectrum. Antenna array consisted of 4 elements with a single source located at angle of 15°. In some situations separation greater than mentioned optimal value may yield precise results for some configurations. However, in some unfavourable conditions, boundary angles or corner cases the setup will provide unreliable data or distorted results.

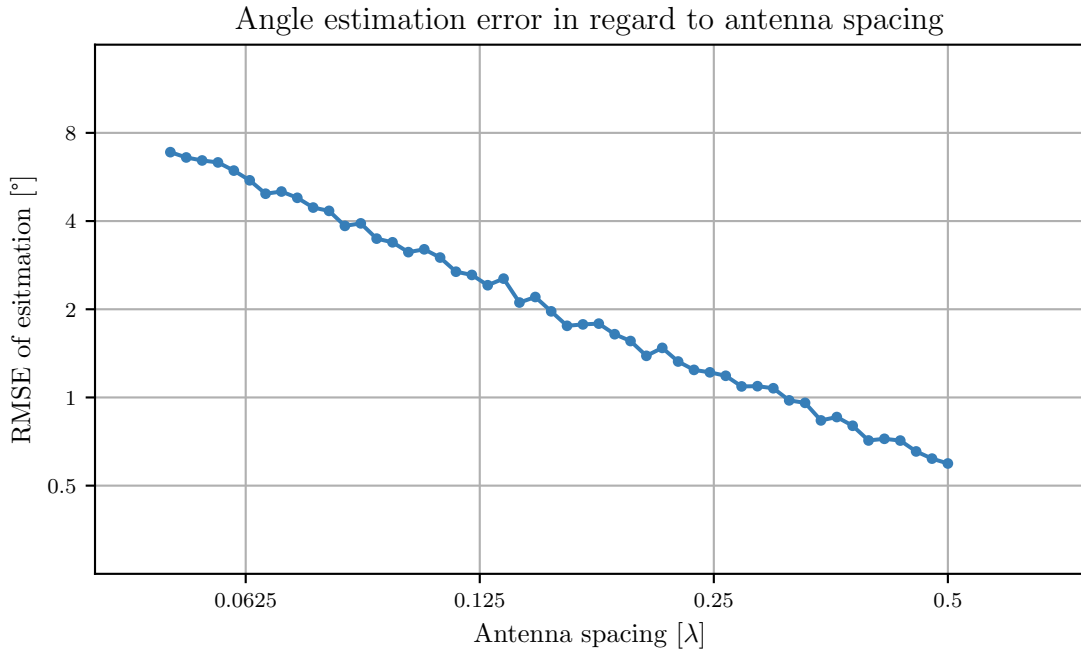


Figure 3.8: RMSE of angle estimation in regard to normalized antenna spacing.

3.2 Hardware and software environment

Implementation and testing of algorithm can be split into two domains: hardware and software. Hardware part consists of choosing the SDR device, constructing the antenna array, providing means of physical angle measurement and wiring of the devices. Software section is associated with

configuration of the devices, implementing signal processing blocks and setting up data flowcharts in SDR toolkit.

Software defined radio platform

As a receiving radio interface employed at the array USRP B210 was chosen, produced by Ettus Research, a National Instruments brand. USRP stands for Universal Software Radio Peripheral, which comes with an extensive software support. It can be used with Matlab, LabView or GNU Radio. Devices are supported via open-source drivers, Ettus Knowledge Base Wiki, broad portfolio of examples and email discussion group.

Key features of USRP B210 [20]:

- 2 RX and 2 TX channels, MIMO capable
- Continuous frequency range: 70 MHz – 6 GHz
- Up to 56 MHz of instantaneous bandwidth (61.44 MSPS quadrature)
- Open and reconfigurable Spartan 6 FPGA
- Fast USB 3.0 connectivity
- Additional frequency and time SMA input enabling synchronization (10MHz, 1PPS or optional on board mounted GPSDO module)

For the transmit node ADALM PLUTO [10] SDR was used. Produced by Analog Devices it has gained popularity as relatively inexpensive software-defined radio module. It can be interfaced with GNU-Radio, Matlab or ADI IIO Oscilloscope. Supported with AD StudentZone, Virtual Classrooms and wiki it has become a common tool for experimentation and learning. Additionally, PLUTO SDR frequency range can be extended from 325 MHz – 3.8 GHz to 70 MHz – 6 GHz and bandwidth respectively from 20 MHz to 56 MHz. It is achieved by changing system environmental variable responsible for compatibility with radio front end chip from AD9363 to AD9364[9]. Upgrade is fully legal, however the manufacturer does not guarantee the RF performance outside of primarily declared frequency range.

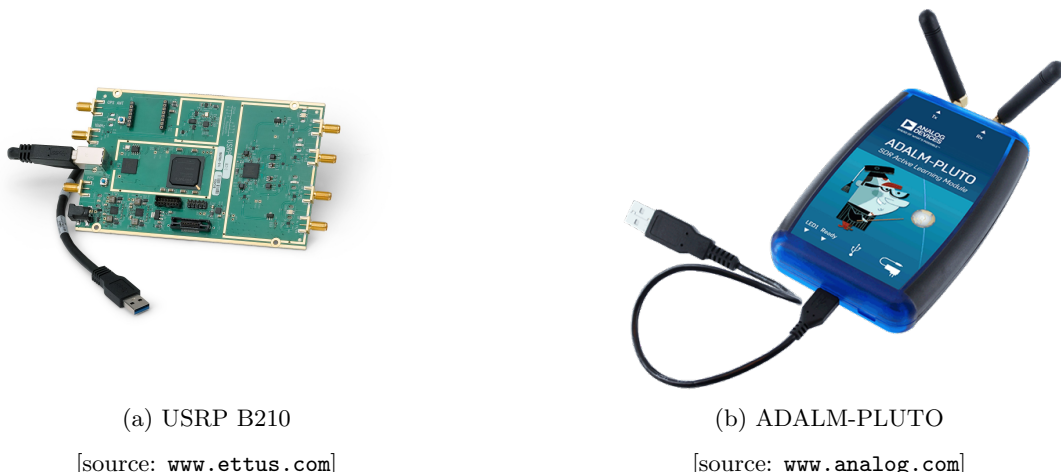


Figure 3.9: Software-defined radio devices used in the setup.

Key features of ADALM-PLUTO SDR:

- Single RX and TX channel, full duplex capable
- Continuous frequency range: 325 MHz – 3.8 GHz
- Up to 20 MHz of instantaneous bandwidth (61.44 MSPS complex I/Q), continuous transfer limited by USB 2.0 speed
- USB OTG and USB 2.0 interface with support of external devices
- Open and reconfigurable Zynq FPGA with Matlab and Simulink support

Phased array construction

Key element of the setup is the antenna array which provides required spacing between antenna elements and secures their positions. The array is designed to work in the center of Bluetooth frequency range. With the boundary frequencies of values 2.402 GHz and 2.480 GHz, the resultant center frequency is equal to:

$$f_{center} = \frac{2.402\text{GHz} + 2.480\text{GHz}}{2} = 2.441 [\text{GHz}] \quad (3.1)$$

Normalized spacing of elements was set to 0.5λ as this value is proven to be the most optimal for AoA estimation as shown in section 3.1. With known target frequency of the array, antenna separation distance can be calculated:

$$d = \frac{c}{2f} = \frac{299,792,458\text{m/s}}{2 \cdot 2,441\text{GHz}} \approx 61,41 [\text{mm}] \quad (3.2)$$

Frame of the array was constructed with aluminium angle profile and simple wooden stands. Single frame can host up to 8 antennas, one of which should be the calibration source. Due to manual methods of drilling 1mm of dimensional uncertainty should be considered.



Figure 3.10: Phased array frame construction.

The frame is equipped with a protractor mounted between middle antenna elements and aligned to the axis of the array. It enables flexible measurement of angle between the array and source node. In order to read the angle a thread is tied to the screw holding the protractor and determining the center of the array. The other end is tied to the source node. Measurement is performed by reading the value crossed by taut thread on the number scale. In case of short distances attention should be paid to the orientation of the knot so that it corresponds to the center of the mounting post or connector, not to introduce any additional angle offset. Phased array construction is presented in Fig. 3.10.

Signal source node

During the measurements the signal source node is moved to various places to obtain the requested AoA, while the array remains fixed. To provide mobility to the greatest extent possible the target source construction was based on a tripod. ADALM PLUTO SDR served as flexible transmitter, which was connected to the central computer via Ethernet. To eliminate additional USB powering cable, Power over Ethernet (PoE) solution was introduced. This configuration provides data and power supply transfer through single 15m long Ethernet cable. Schematic of the source node wiring and construction can be seen in Fig. 3.11 and 3.12 respectively.

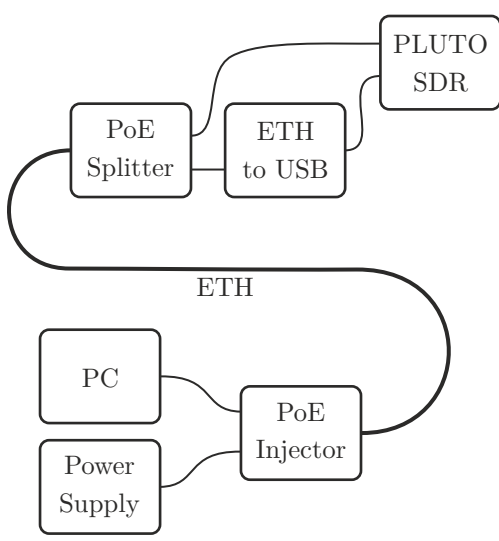


Figure 3.11: Wiring schematic.



Figure 3.12: Source node construction.

Software environment

As a toolkit to control SDRs and process data GNU Radio (GR) [18] was chosen. It is a free and open-source signal processing development framework. The ecosystem is supported by many SDR suppliers as well as a huge community both amateur and academic. In GNU Radio, systems are designed in a form of flowchart diagrams, where signals are processed by blocks that are connected with one another. Designing can be assisted by graphical user interface (GUI) of GNU Radio that provides tools for placing and wiring the blocks. Running the flowchart is also accompanied by GUI for plotting graphs and displaying information. Flowcharts may use external front ends like SDR or operate without any physical interface processing data files or running interactive simulations.

GNU Radio provides infrastructure for developing signal processing blocks in modular approach along with templates, test-cases and documentation. The processing routines of block can be written either in Python or C++. One should keep in mind that Python has a significant performance penalty when it comes to signal processing, due to flexible nature of the language. Although, it is suitable for prototyping and QA tests, well defined algorithms including calculation intensive tasks should be handled in C++. Blocks are represented by boxes with name, most important variables and ports. Their form is determined by descriptive YAML file.

GNU Radio Companion provides graphical environment to create and modify flowgraphs which are stored as files with .grc extension. When the diagram is finished a script containing defined connections, parameters and block references can be generated and executed. Executable scripts are mostly generated in Python, even though some of the blocks were created with use of C++. This is done with help of SWIG, which is a simplified wrapper and interface generator. At the time of writing new GNU Radio release 3.9.0.0 was published, which replaces SWIG with Pybind11. Aim of using these packages is to provide handles to call CPP functions within main Python script. Flowgraph execution script can be easily modified according to needs to integrate required callbacks or implement custom procedures.

Most of operations performed on data in GR utilize vectors. To maximize performance of processor with this type of data special library called VOLK was introduced. VOLK is a Vector-Optimized Library of Kernels, that contains kernels of SIMD (Single instruction, multiple data) code written for several different processor architectures and mathematical operations. The package comes with a profiler that chooses the best SIMD architecture for the processor resulting in reduced computation time. It is worth mentioning that in GR data between blocks is transferred by vectors. Therefore other structures like matrices need to be properly sliced and reconstructed between blocks. This is commonly achieved by adding parameters to block describing number of columns or rows of the data structure.

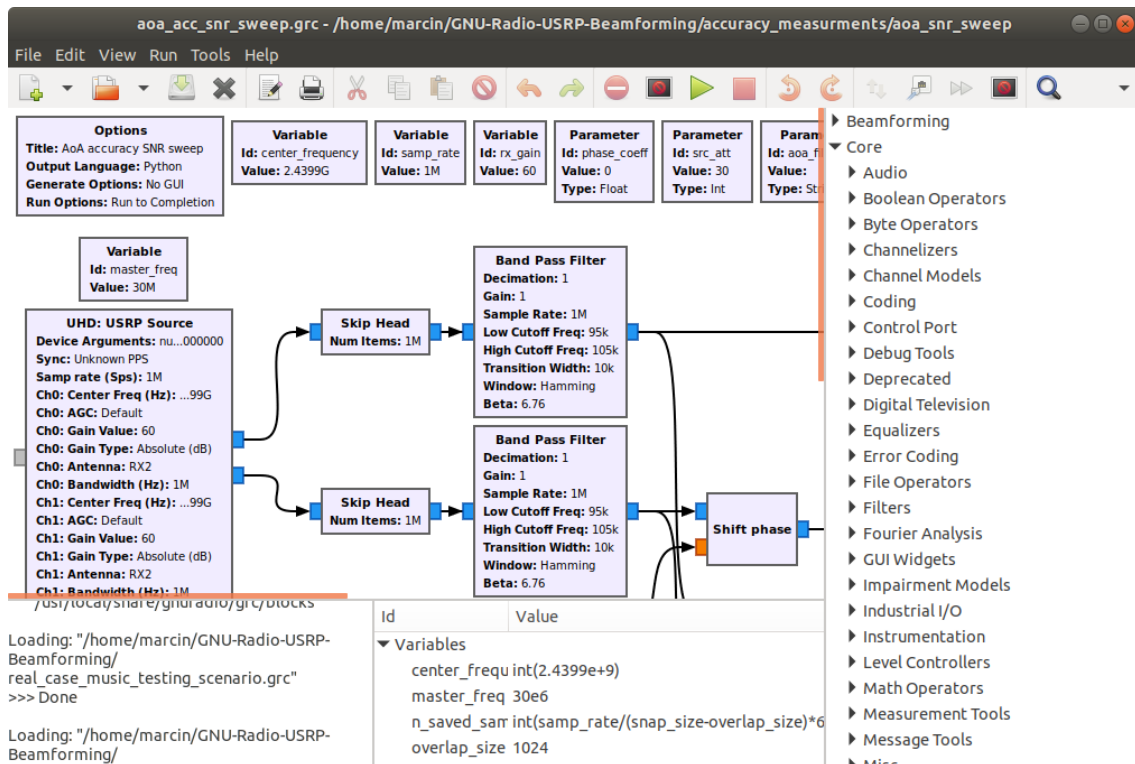


Figure 3.13: Exemplary GNU Radio Companion window with flowgraph.

3.3 Implemented signal processing blocks

Realization of MUSIC algorithm required implementation of a few signal processing blocks that were previously unavailable in the framework. As has been already mentioned Ettus Research provided a GR module: `gr-doa`, that included blocks for MUSIC AoA estimation [24]. This package was aimed at X-Series and TwinRX USRP. Being released for GNU Radio 3.7. the blocks are incompatible with later versions like 3.8 or 3.9 due to changes in API bindings. `Gr-doa` module was based on Armandillo[7], which is a C++ linear algebra library balancing the speed and ease of use. The module contains additional Octave simulation scripts, which were used in testing routines for the implemented blocks and may be useful in generating reference results.

In order improve the performance, some of the `gr-doa` signal processing blocks were rewritten to utilize Eigen [4] library, which is considerably faster. If possible operations on vectors were performed with use of VOLK library. Porting the blocks to the the latest release of GNU Radio enabled reuse of some templates. This resulted in creation of `gr-beamforming` [29] package publicly available online containing all the blocks, flowcharts and analyzes used within scope of this work. Functionality of the blocks has been thoroughly tested with simulation flowcharts. In some cases additional routines needed to be implemented to prevent runtime crashes or unreliable results. List of the blocks with description can be found in Tab. 3.1.

Blocks associated with array calibration: `Calculate phase difference` and `Shift phase` have two instances. Marked with (M) sign in the name, they provide a replicated functionality of their original equivalent with predefined connections and indexing. Number of ports is defined by parameter `Number of signals`, that enables scaling of the blocks. Their implementation is based on hierarchical approach, which allows to replace a repeating fragment of flowchart with an instance of new block. Scalable blocks enable better flowgraph organization resulting in simplification of connections without any performance penalty. Graphical representation of signal processing blocks can be seen in Fig. 3.14.

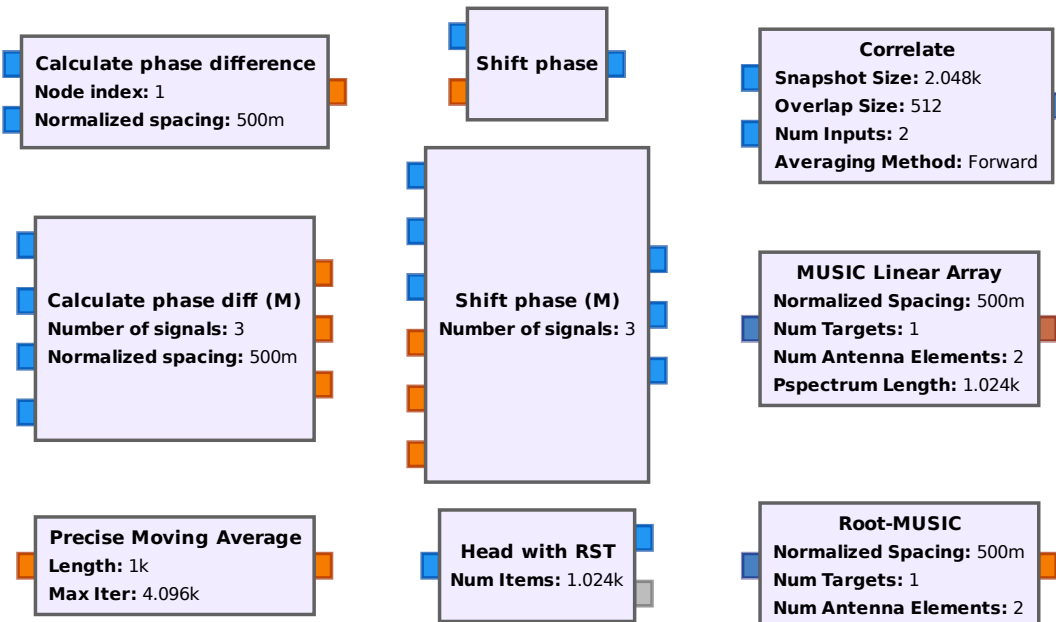


Figure 3.14: Implemented and ported blocks appearance in GNU Radio.

Table 3.1: Implemented or ported blocks.

Name	Property	Description
Calculate phase difference	Function: Input: Output: Parameters:	Determine phase shift required to align signals in ULA using wireless calibrating source located at the end of array. Two streams of complex of samples: reference and input Stream of float values, representing required angle shift in radians Normalized Spacing – spacing of antenna elements expressed in wavelengths, partially determines value of phase shift required for synchronization Node index – index of antenna in regard to first reference receiving element, which designated by 0

Phase shift coefficient required to synchronize phased array is calculated as follows. Suppose that signals received by RX of SDR are $S_{ref}(t) = Ae^{j2\pi ft + \varphi_1}$, which is the calibration signal and $S_{in}(t) = Be^{j2\pi ft + \varphi_2}$. First, the reference signal is multiplied with complex conjugate of the second signal:

$$Y(t) = S_{ref}(t)S_{in}^*(t) = Ae^{j2\pi ft + \varphi_1}Be^{-(j2\pi ft + \varphi_1)} = AB e^{\varphi_1 - \varphi_2} \quad (3.3)$$

As a result we get a coefficient describing phase shift between signals and product of amplitudes. Next, the result is multiplied – shifted by value determined by normalized array spacing to include the phase shift caused by distance between array elements. The phase shift introduced by distance traversed by EM wave is calculated according to (2.47).

$$Y_{corr} = Y e^{j2\pi \frac{d}{\lambda} n_i} = AB e^{(\varphi_1 - \varphi_2 + j2\pi \frac{d}{\lambda} n_i)} \quad (3.4)$$

Where $\frac{d}{\lambda}$ is normalized antenna spacing expressed in wavelengths, and n_i is the node (receiving element) index. Reference antenna has index of 0. Finally, the combined phase shift coefficient is converted to radians:

$$\varphi_{corr}[rad] = \arctan(Y_{corr}) \quad (3.5)$$

Analyses presented in continuous time domain also apply to discrete signals – represented by complex samples. In this case t argument should be replaced with k designating a discrete moment in time.

Shift phase	Function: Input: Output: Parameters:	Shifts each sample in phase by value provided at the input Stream of complex signal samples and a stream of float values representing the phase shift in radians Complex stream of shifted signal samples –
-------------	---	--

Signal is shifted in phase by provided value $\{r\}$ in a following way. Suppose that input signal is expressed as $S_{in} = Ae^{j2\pi ft + \varphi_1}$. Shifting the signal phase is achieved by multiplying it with complex coefficient obtained from Euler's formula:

$$S_{out}(t) = S_{in}(t)e^{jr} = Ae^{(j2\pi ft + \varphi_1 + r)} \quad (3.6)$$

Name	Property	Description
Correlate	Function: Input: Output: Parameters:	Generate sample correlation matrix from input sample vectors N complex sample streams Complex correlation matrix of size $[N \times N]$ transferred in a form of a vector Snapshot size – length of vector of samples to be correlated Overlap size – length of vector of samples shared between subsequent calculations Num inputs – number of input sample streams Averaging method – "Forward" or "Forward-Backward" method of calculating the correlation matrix

Methods of calculating the sample correlation matrix have been discussed in section 2.2:

Forward – standard averaging as expressed in (2.18)

Forward-Backward – with use of additional reflection matrix according to (2.19)

MUSIC Linear Array	Function: Input: Output: Parameters:	Calculate AoA pseudospectrum using MUSIC algorithm Correlation matrix of complex type transferred as a vector Pseudospectrum vector of specified size of floats Normalized Spacing – spacing of antenna elements expressed in wavelengths Num of targets – number of sources to estimate their AoA Num of antenna elements – number of receiving elements Pspectrum length – length of pseudospectrum vector
--------------------	---	--

Size of pseudospectrum vector determines number of tested AoA values, equally distributed in range from 0° to 180° . The resolution of returned results is $\Delta = \frac{180^\circ}{v}$, v – length of vector. Returned spectrum values are normalized in regard to maximum found in pseudospectrum vector and converted to decibel scale.

Root-MUSIC	Function: Input: Output: Parameters:	Calculate K angles of sources specified by Num Targets using Root-MUSIC algorithm Correlation matrix of complex type transferred as a vector Vector of K angle values sorted in ascending order Normalized Spacing – spacing of antenna elements expressed in wavelengths Num of targets – number of targets to estimate their AoA Num of antenna elements – number of receiving elements
------------	---	--

Returned estimated angle values are expressed in degrees. First roots, located closest to the unit circle on the inside are selected, if more are required then, the ones closest to the outside are picked.

Name	Property	Description
Precise moving average	Function:	Moving average filter of specified length
	Input:	Stream of float samples
	Output:	Stream of averaged float samples
	Parameters:	Length – Length of averaging window Max Iter – Number of elements accumulated in the buffer of the block before processing them by function

Value of outputted sample is expressed as:

$$\bar{p}_n = \frac{1}{N} \sum_{i=1}^N p_i$$

where, N is the length of averaging window and p_i is the i th sample in the collected vector. This block in comparison to **Moving Average** block already available in GNU Radio has a accumulator of type **double**. Increased precision provides stable performance even for window lengths of 100M samples.

Head with RST	Function:	Collect number of samples specified by Num Items and stop streaming
	Input:	Stream of any data of any type
	Output:	Stream of any data of any type and message output port signalling state of the block
	Parameters:	Num Items – Number of samples to be collected and forwarded to output.

This block has a **reset()** callback, that enables to restart the process of collecting samples, during runtime of GNU Radio script. This functionality provides handles to automate measurement routines. Status of the block is signalled by three messages: **RESET**, **IN PROGRESS** and **FINISHED**.

3.4 Flowgraph scenarios

GNU Radio environment provides great flexibility in regard to testing and evaluation of signal processing systems. Flowcharts can be executed with graphical interface to provide interactive analysis or in a windowless form to process data with predefined settings.

Flowgraph diagrams created throughout the work can be divided into 5 groups:

- Blocks testing – focused on verifying correctness of the operations performed by newly implemented blocks. Help to eliminate unexpected behaviour and expose bugs if present.
- Algorithm simulation – diagrams performing MUSIC algorithm in an interactive way, with parameters controlled by GUI. Results returned by the algorithm can be evaluated in real time. Simulation flowcharts created in GR are different from those presented in section 3.1. Their main aim was to provide basic interactive evaluation of MUSIC algorithm.

Simulation flowchart depicted in Fig. 3.15 is built from following sections. First the signal sources are summed with noise to reconstruct real case scenario. Next the signals are mul-

tiplied by an array manifold matrix created for an arbitrary selected angle of arrivals. The vector and required phase shifts are calculated by single line expressions with help of NumPy package according to (2.4). Output of this operation provides N signals shifted in phase as if they arrived at different antenna elements from chosen directions. Then additional phase noise is introduced to further corrupt the signals. Resultant waveform arrives at the correlation block, where sample correlation matrix is calculated and forwarded to **MUSIC Linear Array** and **Root-MUSIC** blocks. The results returned by AoA algorithm blocks are displayed in a form of plot and bar graph presented in Fig. 3.16.

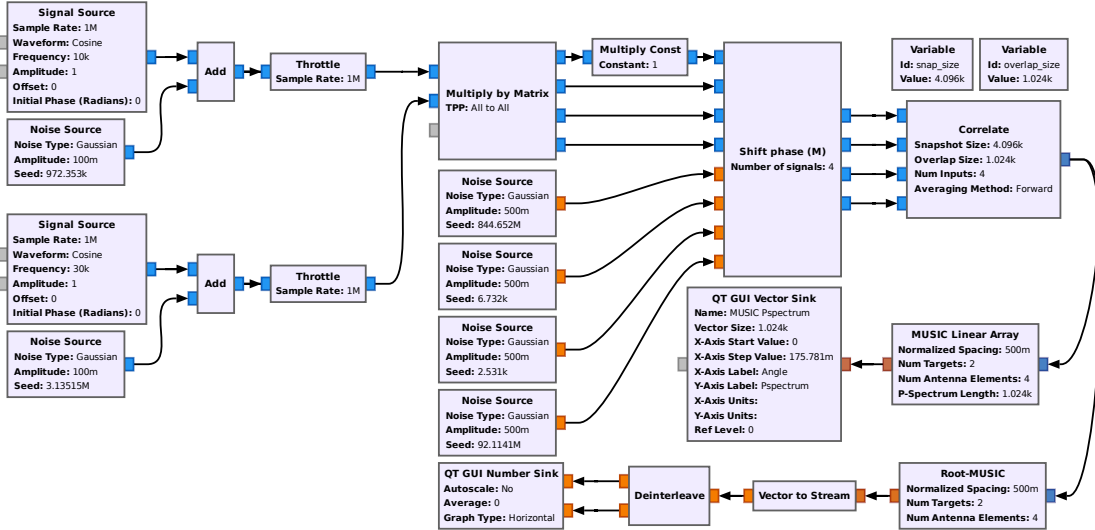


Figure 3.15: GNU radio MUSIC simulation flowchart with 2 sources and 4 antennas.

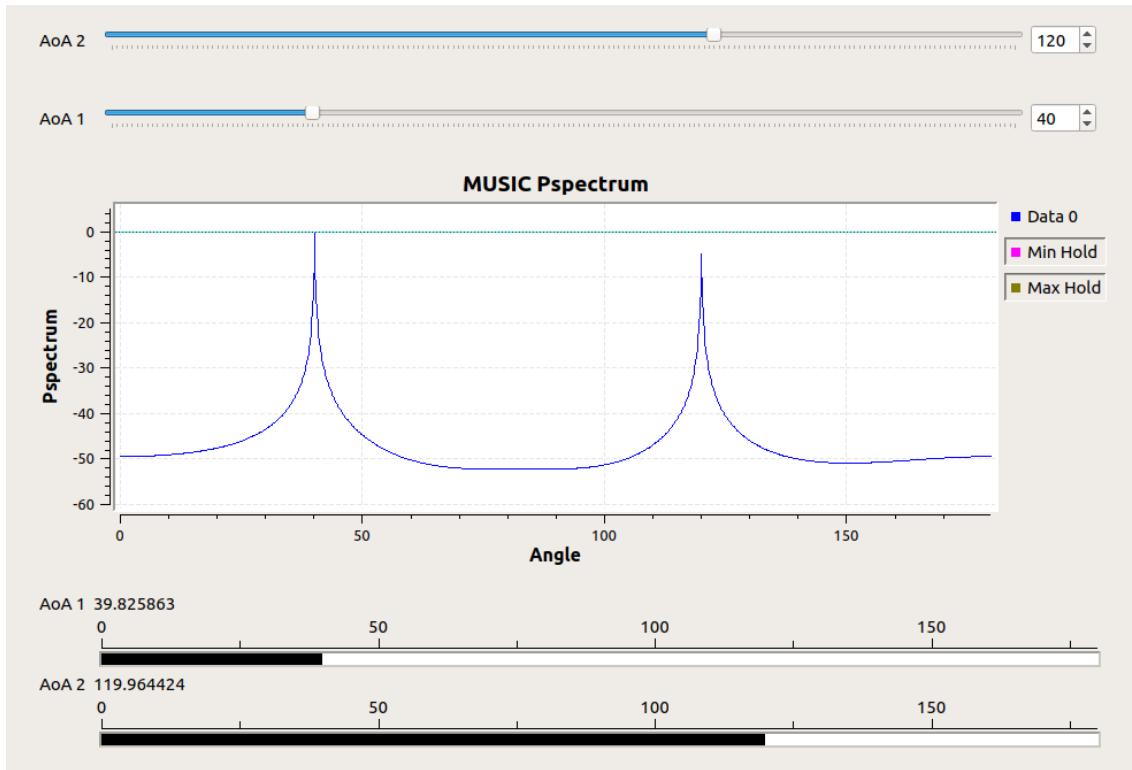


Figure 3.16: GNU Radio MUSIC simulation graphical interface.

- Interactive analysis – flowcharts interfaced with SDR devices, which provide data to be processed by algorithm. Accompanied with extensive graphical interface to visualize the results at different stages of signal processing. Exemplary flowchart used for MUSIC algorithm evaluation can be seen in Fig. 3.17 along with its GUI presented in Fig. 3.18.

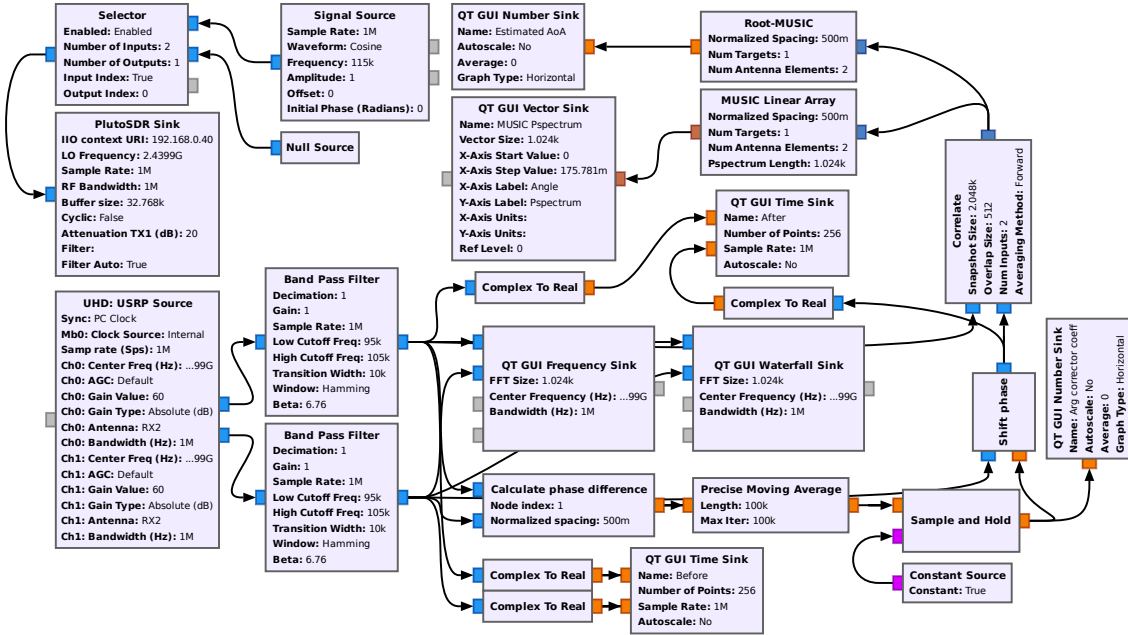


Figure 3.17: Interactive MUSIC algorithm flowchart.

Interactive analysis of MUSIC algorithm in real conditions with use of SDR devices provided an insight what kind of limitations are introduced by hardware and real radio environment. What is more, some of the results obtained by experimenting with the setup resulted in changes introduced to methodology of measurement, calibration and solutions to encountered problems.

- Measurement – similar to interactive analysis, with additional procedure of saving raw IQ samples or processed data to file. Usually with reduced GUI to present only absolutely necessary parameters.
- Raw data processing - flowcharts with no graphical interface, created with option `run to completion`. Variables of the diagram are exposed as command line parameters, including the names of IQ files serving as signal sources and a file to store the output. Resultant executable python file can be used with custom scripts that automate the processing or perform parameter sweeps. Idea of saving raw IQ samples ensures safety that even if the final results were distorted by a setting of block, it is always possible to rerun the signal processing with different parameters.

For the offline processing of IQ data two flowcharts were created. First one to calculate phase correction coefficient with variable moving average window length. Second performs MUSIC algorithm on saved IQ data streams and measures estimation error. Diagram of the latter is presented in Fig. 3.19. Flowgraphs can be launched with variable parameters like phase correction coefficient, correlation snapshot and overlap size. Band-pass filters present in the setup serve to separate the signal of interest from interference present in the band and are discussed later in the measurements section 4.1.

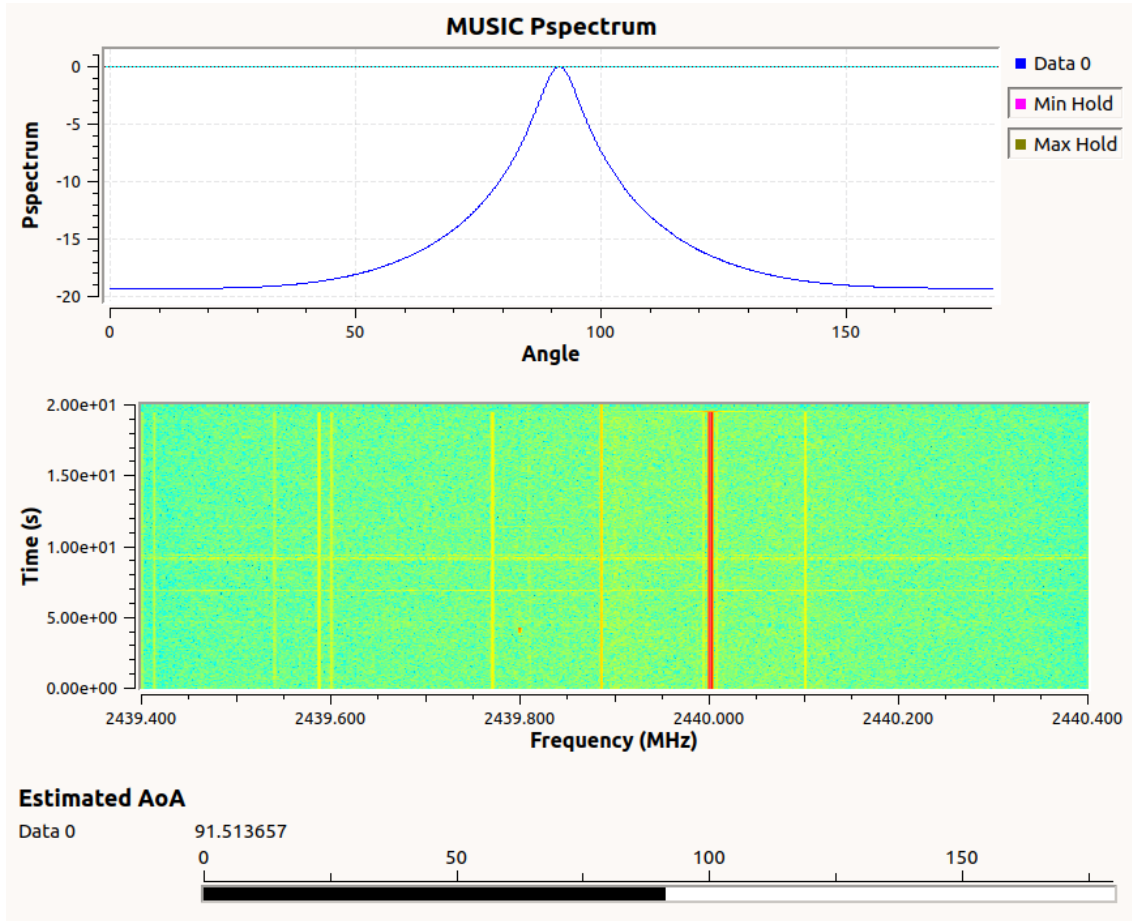


Figure 3.18: Exemplary interactive MUSIC algorithm GUI.

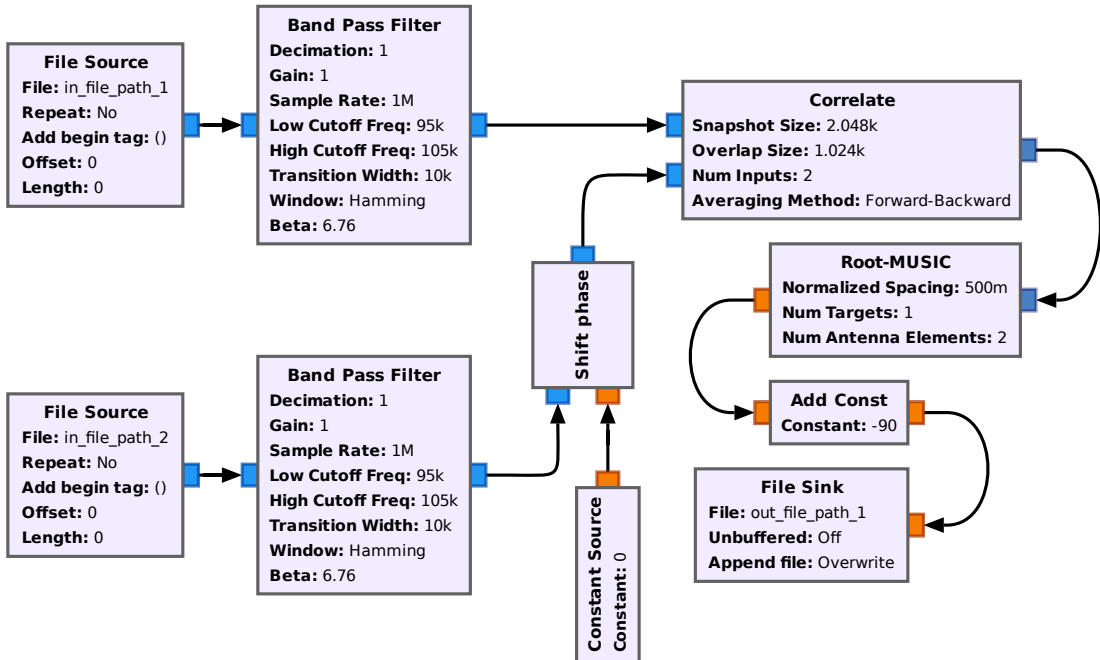


Figure 3.19: Raw data processing flowgraph estimating AoA from prerecorded IQ samples and saving difference in regard to provided physical angle value.

3.5 Wireless calibration routine

One of this work aims is to provide a reliable array synchronization routine through wireless channel. USRP B210 RX and TX channels are already synchronized in frequency and time domain as they are connected to the same LO and FPGA processing unit. However, the phase of radio front-ends synthesizers are offset to each other, with a value that needs to be determined and compensated. The phase offset between channels is introduced due to hardware construction. Manufacturing inaccuracies, limited tolerance of components and asymmetries all contribute to this error.

The experimental setup calibration was performed with single tone of identical frequency as the testing signal. Frequency of both signals was set to be 2.44 GHz with sample rates of 1 MSPS. As has been reported by [11] phase shift between channels of agile transceivers used in USRP is subject to local PLL oscillator frequency. Relationship between these parameters is approximately linear. Phase difference between channels of USRP B210 remains relatively similar between power-cycles of the device. However, temperature and other environmental factors may still affect the value introducing an error.

Initial assumptions were that a single USRP B210 will be sufficient to create a self contained system with two receiving elements and a calibration source utilizing one of TX channels. Throughout numerous tests and comparison of results it has become clear that crosstalk present between RX and TX renders some error. Explanation of the origin of the crosstalk in USRP B210 can be seen in Fig. 3.20.

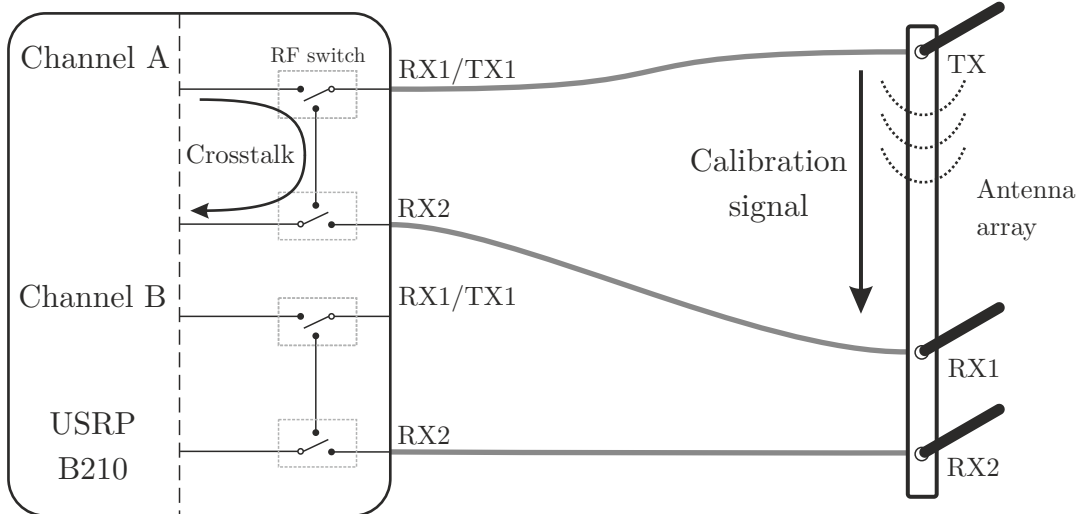


Figure 3.20: Origin of the crosstalk present during phase calibration of USRP B210.

Signal received by the channel with crosstalk can be expressed as:

$$s(t) = Ae^{j2\pi ft} + Be^{j2\pi ft+j\varphi} \quad (3.7)$$

where $Ae^{j2\pi ft}$ is the signal received by RX chain through antenna (wanted) and the second component is the leaking signal that is shifted in phase by φ in regard to the first component (unwanted signal). After the downconversion of the signals, carrier frequency component is removed:

$$s(t) = A + Be^{j\varphi} \quad (3.8)$$

Assuming that in no crosstalk case antenna receives only signal A , which is of real value, the maximal phase shift introduced by B is when it is of purely complex value $-jB$ or $+jB$. The difference in phase is maximal when $B^{ej\varphi}$ complex representation is perpendicular to A in polar coordinate system.

The maximal phase error can be then calculated basing on formed rectangular triangle as:

$$\Delta_\psi = \arctan \left(\frac{B}{A} \right) \quad (3.9)$$

When $B \ll A$ the value of arctangent can be approximated with Maclaurin-Taylor series for tangent resulting in:

$$\Delta_\psi \approx \frac{B}{A} \quad (3.10)$$

During tests performed at frequency of 2,44 GHz, RX gain of 60 dB and TX gain of 40 dB signal that leaked from TX to RX path constituted 0.1 of amplitude received by an antenna. Substituting the measured cross-talk of 0.1 of the main signal to the derived equation the calibration coefficient should be shifted by ± 0.1 rad in worst case. Phase error observed by the tests confirmed the analysis fitting within the calculated range.

Due to this effect antenna array required an independent source to perform calibration. This problem was solved by employing ADALM PLUTO as the source node to generate phase synchronization signal. Calibration antenna was mounted at the array with an SMA pigtail extension. For the synchronization phase the TX antenna was placed at known position in the array. This process involves changing connections and switching of the device.

Originally, the spacing between reference TX antenna and adjacent receiving antennas was of equal length. Phase shift coefficient returned by such calibration did not yield reliable values. Replacing the synchronization antenna with equivalents designated for similar frequencies produced different phase shift coefficients. The same test performed with the TX antenna placed at most distant position in the array, about 40 cm from the first element, returned results of much lower variance. This analysis points to a conclusion that in case of wireless synchronization, receiving antennas should be placed within the far field range of the TX antenna. Near field region and transition zone may be dependent of antenna construction. What is more, problematic nature of the EM field interactions within this region will cause the phase shift coefficient to be incorrect.

To ensure that RX antennas are placed within the far field regime Fraunhofer distance is calculated. It is valid for antennas larger than half-wavelength of the radiation they emit:

$$d_f = \frac{2D^2}{\lambda} \quad (3.11)$$

where d_f is the Fraunhofer distance that defines the beginning of the far field zone, D is the largest dimension of the antenna and λ is the wavelength of emitted radiation.

Substituting the real values used in setup into the formula: $D = 15$ cm and $f = 2.44$ GHz we get:

$$d_f = \frac{2 \cdot 0.15^2}{\frac{3 \cdot 10^8}{2.44 \cdot 10^9}} = 0.366 \approx 37 [cm] \quad (3.12)$$

Chapter 4

Measurements

4.1 Stability of phase calibration

Stability of phase calibration is of key importance in an angle of arrival estimation system. Coherence provided by synchronization routine may be distorted by slow drift or variable offset introduced by hardware heat up or settling time. To verify the scale of possible error introduced by temperature change a series of measurements of phase and amplitude coefficients were performed. During the measurements no movement was present in the room unless noted otherwise. System operated at frequency of 2.44 GHz and at times at 2.45 GHz to verify its performance in congested band. Phase synchronization and source signal were a single tone with baseband frequency equal to 100 kHz. To properly observe and filter the signals SDR devices center frequency was set to respectively to 2.4399 GHz or 2.4499 GHz.

Firstly the phase correction coefficient drift, which represents phase shift required to align signals in the array, was observed with the use of wired setup. Signal from calibration source was fed to RX ports through attenuator and splitter with cables of matched length. Measurements were

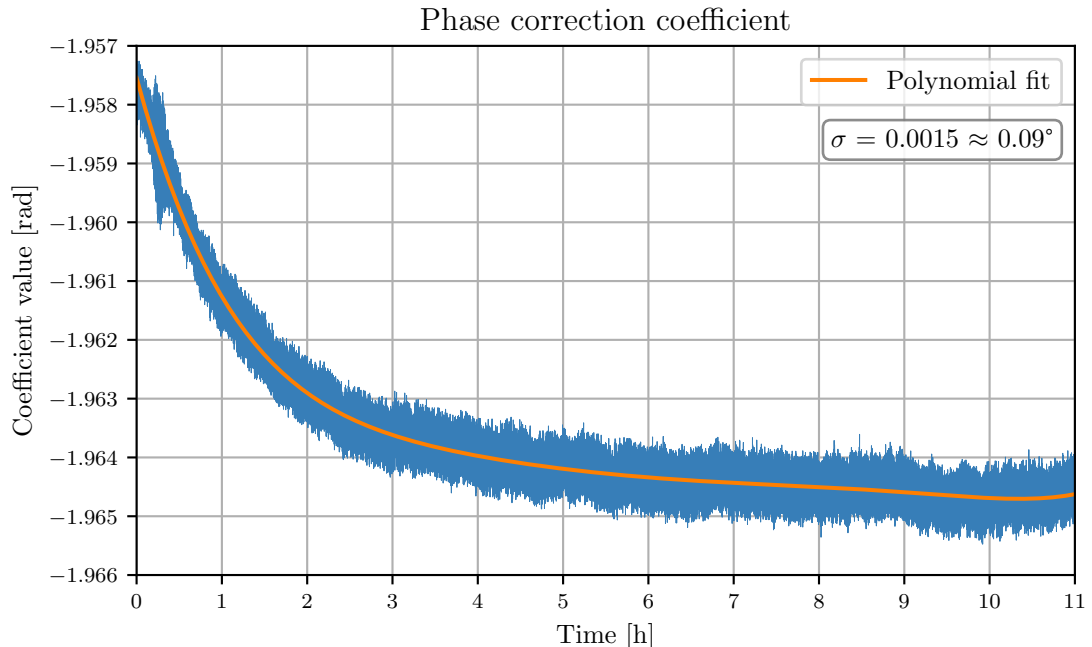


Figure 4.1: Reference phase shift correction coefficient drift.

performed for previously unpowered devices to observe the extent of phase shift change introduced by heat up and measure the settling time. As the coefficient values can be unstable and susceptible to distortions moving average (MAV) filter was introduced to reduce the variance of the results. Initially MAV filter with window length of 1k samples was used.

The constant component of the phase shift coefficient is to be neglected as the setup did not include phase shifts associated with antenna elements spacing. Only the shape and relative change is relevant in this case. As can be noted from Fig. 4.1 heat up can introduce an error of up to $0.007 \text{ rad} \approx 0.4^\circ$ to the value of phase calibration coefficient. The drift remains present for a few hours from powering on the devices and small fluctuations may occur after it has stabilised. Observed standard deviation of the phase shift is 0.09° , which is relatively small value, that should not impact AoA accuracy in any significant way.

Next, similar measurement was performed with the use of antennas. Array was synchronized via wireless channel by a single tone at frequency of 2.44 GHz. Several lengths of moving average filter were used to evaluate how it influences the stability of the coefficient. Results presented in Fig. 4.2 show that the phase coefficient value is relatively stable. Its error is in the range of about $\pm 0.005 \text{ [rad]} \approx 0.29^\circ$ for MAV filter of length over 100k samples. Increasing the moving average filter length does not yield any substantial reduction of coefficient standard deviation.

In order to observe how high activity in the channel affects phase synchronization of the array center frequency of the system was shifted to 2.45 GHz. To increase the occupancy of the band video transmission was active on the central computer connected to local Wi-Fi network. The analysis included evaluation of MAV filter length and band-pass filtering. ISM band is occupied with various wideband transmissions that overlap with the working frequency of the setup. Application of band-pass filtering should reduce the out-of-band and adjacent-channel interference. Filter used in the setup was of FIR type with frequency range of 95–105 kHz and transition width of 10 kHz. Comparison of measured coefficient variance values can be found in Tab. 4.1 and graphical representation of coefficient fluctuations in Fig. 4.3.

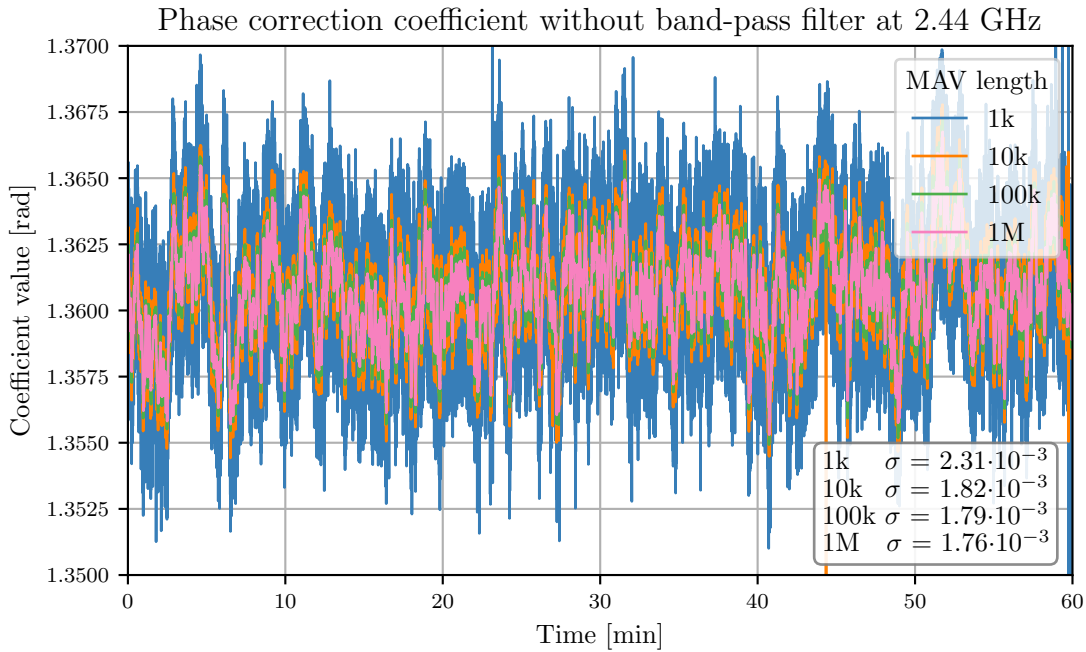


Figure 4.2: Stability of phase correction coefficient at 2.44 GHz

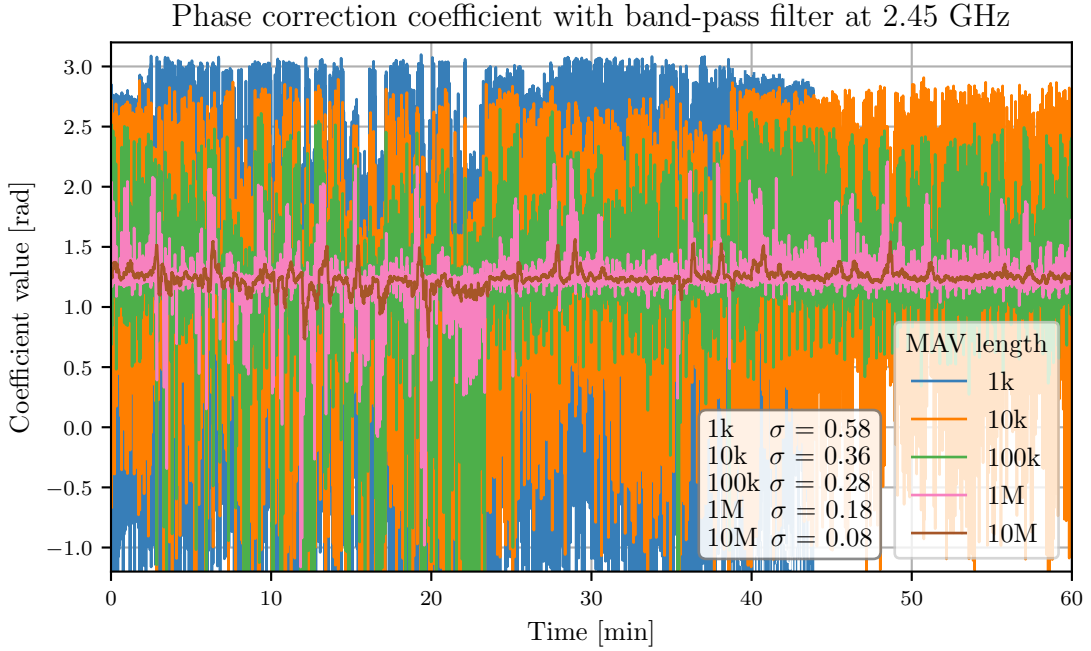


Figure 4.3: Stability of phase synchronization through busy wireless channel at 2.45 GHz.

MAV length	Phase coefficient standard deviation [rad]	
	not filtered	band-pass filtered
1k	0.69	0.58
10k	0.62	0.36
100k	0.56	0.28
1M	0.38	0.18
10M	0.15	0.08

Table 4.1: Phase coefficient standard deviation in busy wireless channel.

In contrary to previous measurements, high activity in the wireless channel is proven to greatly distort phase coefficient. Transmissions present in the ISM band interfere with the synchronizing tone introducing significant deviances from true value. The range of variability can be reduced by applying band-pass filtering, which effectively suppresses signals located at neighbouring frequencies. Introduction of filter reduces coefficient amplitude fluctuations approximately by factor of 2, for MAV length over 1k. Combined with moving average filter it is capable of providing synchronization of standard deviation of $0.08 \text{ [rad]} \approx 4.6^\circ$. Extending the length of MAV and selectivity of the filter has a positive influence on the precision of calibration, however it requires much more computational resources.

Transmission in wireless channel is accompanied by numerous impairments and distortions introduced by interactions with the physical environment. One of the key phenomenon affecting the quality of transmission in wireless channel is multipath propagation. Obstacles surrounding the antenna may reflect, refract or diffract the signal resulting in interference. As a result received signal is a sum of components arriving through different paths, with various amplitudes and phase shifts. To determine how vulnerable is phase correction coefficient to multipath effect and changes of propagation in environment appropriate measurement was performed. During the test movement was introduced by a person walking close to the array. Results of the measurement are presented in Fig. 4.4.

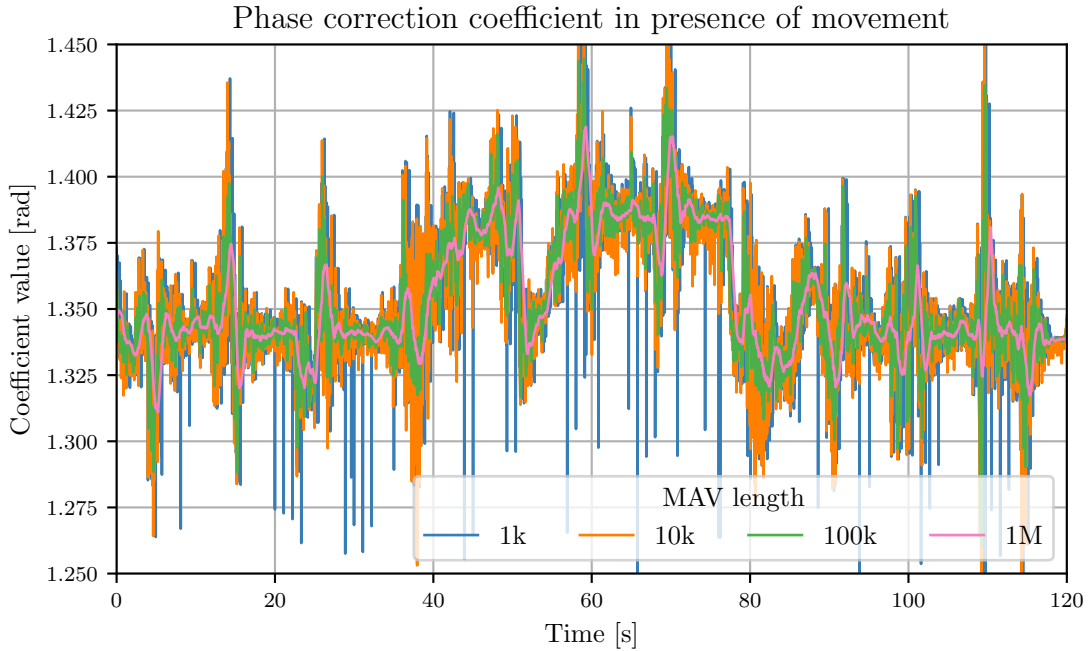


Figure 4.4: Stability of phase correction coefficient in presence of movement in the room.

It can be seen that movement of single person can cause up to $0.1 \text{ rad} \approx 5.7^\circ$ of phase error. Therefore, it is crucial that the synchronization routine should be performed in an environment with limited movement. It also important that the distance to the closes obstacle should be at least greater than separation of TX and RX antennas to limit the present multipath phenomenon.

Relative gain drift and difference

To verify the scale of difference in receiver sensitivity, additional measurement was performed. Signal source was connected to RX ports through an attenuator and splitter. First RX channel served as reference and the value of power received at second channel was divided by the reference to obtain *power correction coefficient*. Gathered results are shown in Fig 4.5. Measured difference in received power is of about 1 dB. It should be noted that in case of wireless sensitivity calibration of ULA, attenuation introduced by distinct spacing of each RX element from TX antenna needs to be taken into consideration.

The disparity may become even greater in unfavourable multipath conditions or by dissimilarities introduced by wiring and antennas. MUSIC algorithm requires that noise power received at each node is equal, however taking into consideration mentioned imperfections and phenomena, calibration of the array in regard to received power may be hampered and pose a limitation in regard to the setup performance.

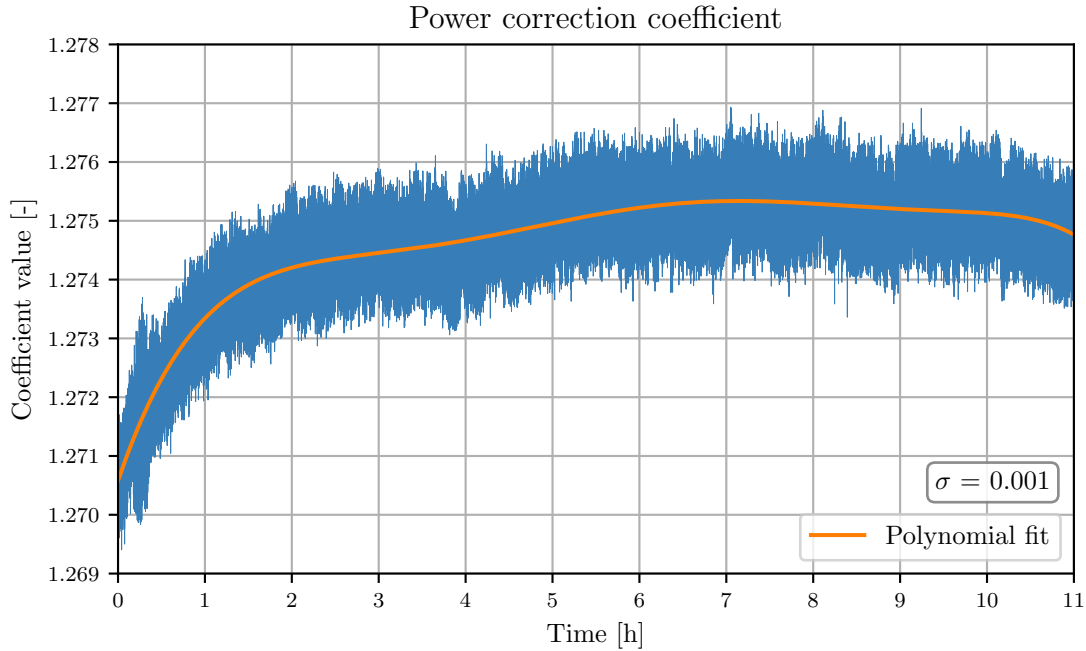


Figure 4.5: Received signal power difference and drift.

4.2 Accuracy evaluation

Before performing field tests and measurements in a large hall, results returned by MUSIC algorithm were evaluated for different settings and conditions. The transmit node was placed at an angle of 90°, 2 m from the array. Angle estimation was performed for 60 s with 1 MSPS rate and snapshot length of 1024 which resulted in about 58k of angle values. Figures 4.6 – 4.9 comparing returned results under various conditions have mean of their data set subtracted to better visualize the variability of angle estimation.

Initial analysis focused on angle estimation error introduced by interference present in the band of interest. Measurement was performed for two different states of the channel, first with normal activity in the band and second one with high traffic in the wireless network. The network traffic was generated by activating a video streaming service on the computer connected to local Wi-Fi network. Obtained results are presented in Fig 4.6. The results demonstrate that high activity in the 2.4–2.5 GHz ISM band greatly increases variance of angle estimation error. The range of values is extended to $\pm 2^\circ$ and the occurrence of significant error is packet-like. As is shown in the plot the root mean square error increases in busy channels.

Next analysis evaluated the validity of band-pass filtering in scenario with high interference in the band. The position of the source and array remains as in previous case. Parameters of the filter were similar to the one present in phase calibration: FIR type, frequency range 95–105 kHz and transition width of 10 kHz. The setup employed two branches in the same flowchart one with filtering and one without to simultaneously process the data. Gathered results are presented in Fig. 4.7. To better visualize the differences in some cases secondary plot may be replicated to provide reference for comparison. Graphs obtained from analysis of filtering impact on accuracy of estimation prove, that band-pass filtering is absolutely necessary to limit the interference from overlapping bands in busy wireless channel. Error values introduced by other transmissions spread the whole range of estimation [0–180°]. The RMSE of angle estimation without filtering is at unacceptable level of approximately 8°.

Estimation error in regard to activity in wireless channel at 2.45 GHz

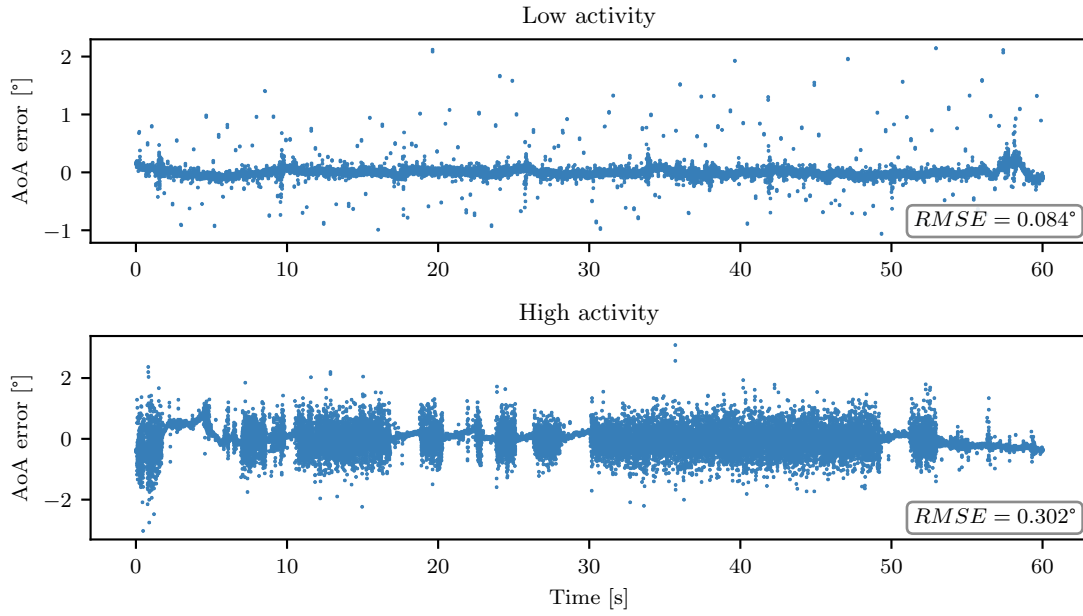


Figure 4.6: Comparison between AoA estimation error in channel with high and low activity level.

Effect of band-pass filtering on estimation error at 2.45 GHz

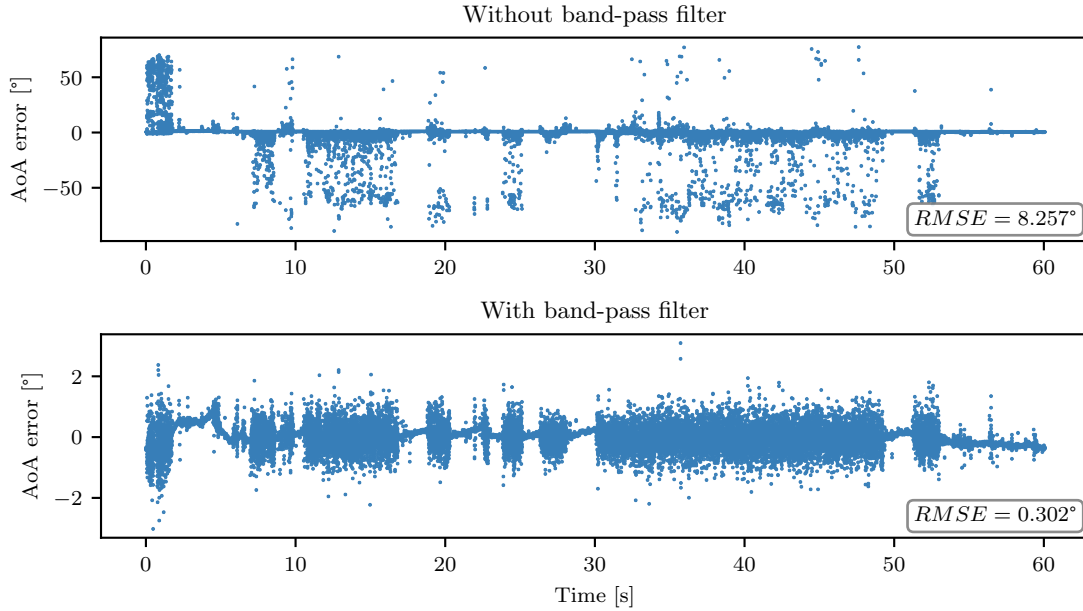


Figure 4.7: Effect of band-pass filtering on AoA estimation in busy channel.

Subsequent measurement was aimed at investigating how movement distorts the angle of arrival estimation. As has been previously presented in Fig. 4.4 phase shift coefficient is susceptible to changes in multipath environment. Results were gathered with applied band-pass filtering and low activity in the frequency range. Movement was introduced by a person walking around the source and array – not crossing the line of sight. Results of this analysis are present in Fig. 4.8.

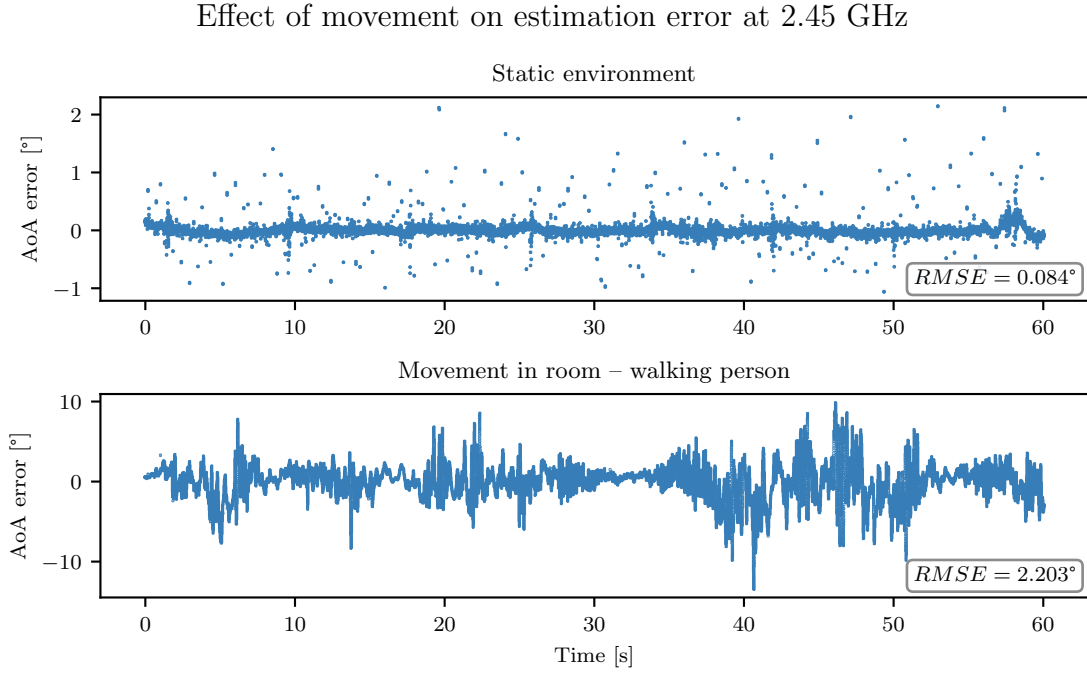


Figure 4.8: Effect of movement present during AoA estimation in channel with low activity.

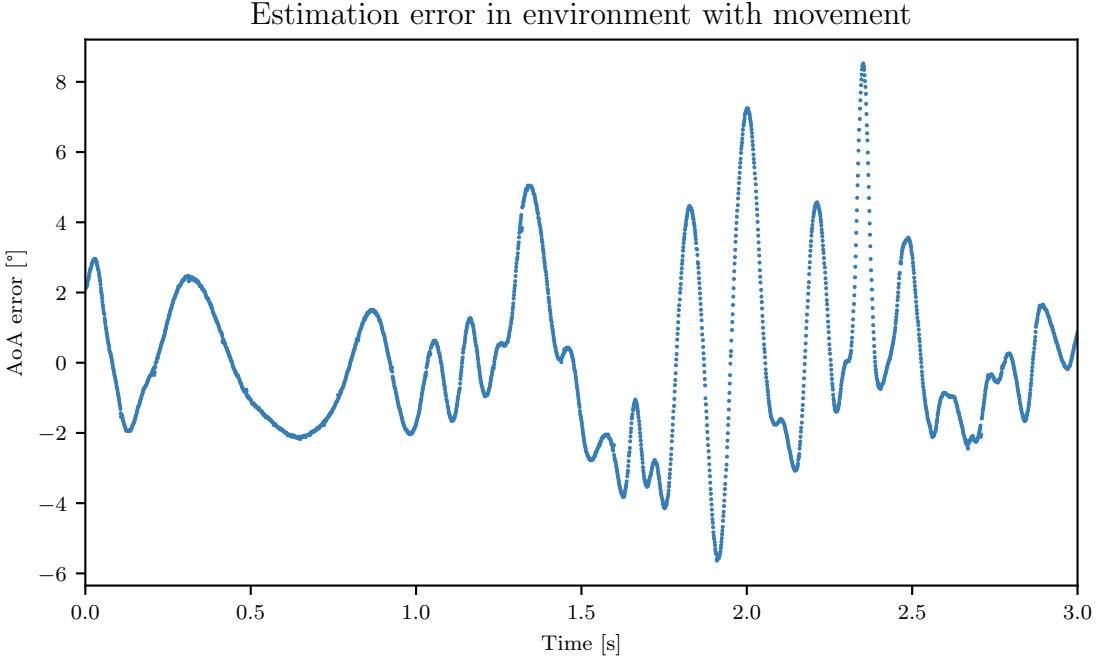


Figure 4.9: Effect of movement on AoA estimation during short period of time.

Estimation error introduced by movement dominates other sources and ranges between $\pm 10^\circ$. Changes in value correspond to the movement of the person and even smallest activities like breathing or nodding are recorded in the estimated angle value. The characteristic shape of changes introduced by movement in a short period of time can be seen in Fig. 4.9. Distortions present in estimated value have a specific harmonic nature and locally resemble sinusoidal function with additional components.

Last analysis consisted of verifying how estimation value and its variability depend on the signal to noise ratio in real radio environment. Measurement was performed with band-pass filtering, source was located at 90° 2 m away from the array. First, noise present in the band was measured and averaged to obtain a reference level for 60 s. Then a series of measurements of AoA and received signal power were performed for various **source attenuation** settings of PLUTO SDR also for time interval of 60 s. For sample rate of 1M this resulted in about 58k values of AoA values and 60M samples of squared signal magnitude. Obtained signal powers were averaged and compared with noise to calculate signal to noise ratio. Estimated angle value and its variability in regard to SNR is presented in Fig 4.10. The error bars represent the standard deviation of the measured AoA value.

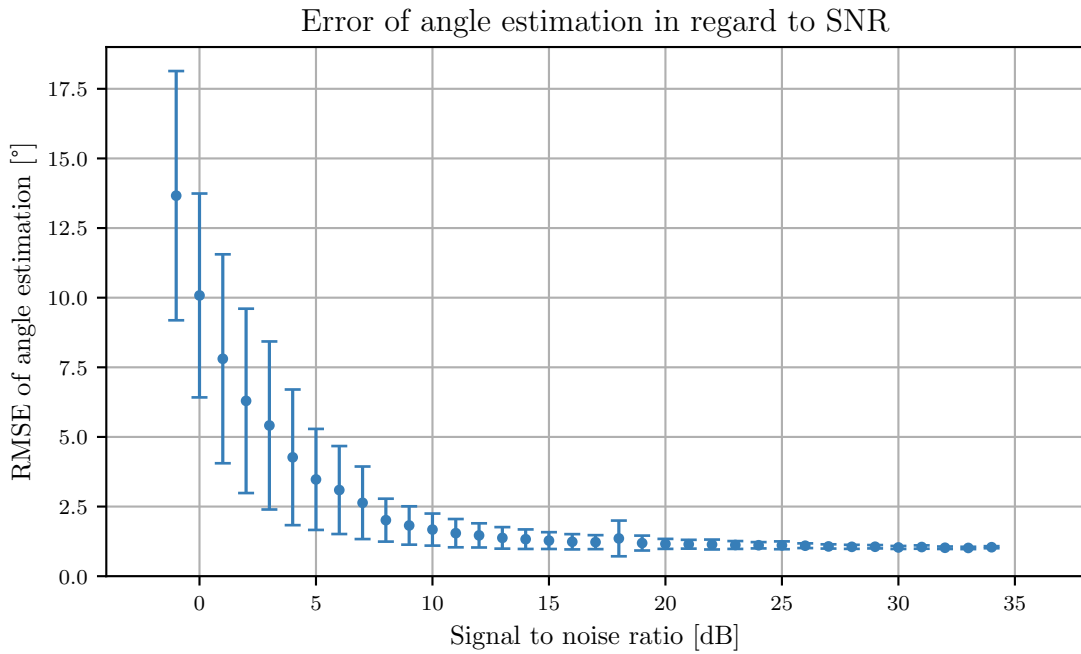


Figure 4.10: Estimation accuracy in regard to signal to noise ratio.

Plotted dependency shows that low values of signal to noise ratio contribute to greater value of error and variance of estimation. Obtained results are partially similar to the simulation results presented in section 3.3 in regard to the initial range of SNR values. From value of about 15 dB further increase in signal to noise ratio does not yield any significant enhancement of accuracy.

4.3 Field tests

Accuracy of the setup was verified by tests in within real radio environment with source placed at angles within the range of $[10\text{--}170^\circ]$ and distances of 1 to 5m. Measurements were performed in two locations, first one being gymnasium and local performance hall. The setup operated at frequency of 2.44 GHz with active band-pass filtering. Antenna array was fixed while the source node was moved around to selected angles. The setup is presented in Fig. 4.11. Measurement for each position consisted of saving the estimated angle values and raw data from each RX front end for 60 seconds. (This resulted in 60M samples of raw data for each channel and about 58k of angle estimation values assuming snapshot size of 1024.)

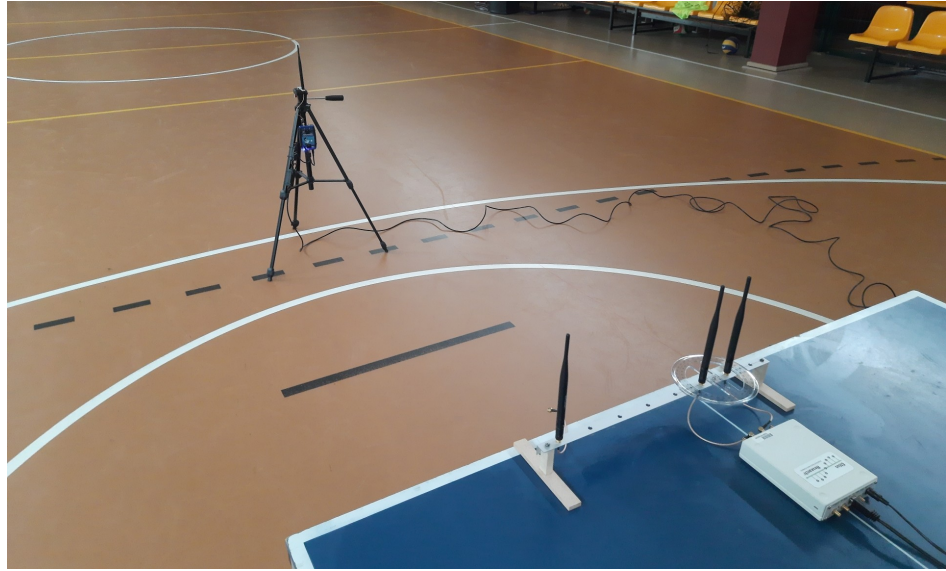


Figure 4.11: Measurement setup used in evaluation of algorithm accuracy.

First series of measurements was performed in a sports hall for distances ranging from 1 to 3m. Obtained results are presented in Fig. 4.12, plotted points represent averaged value of estimation error and error bars correspond to standard deviation of each measurement. Accuracy of angle estimation is vitiated by relatively significant error. For some cases the error is as large as 20° . Overall averaged root mean squared error of all results is approximately equal to 11° . However it should be noted that the setup consists of only 2 receiving antennas and due to this fact it is very sensitive to multipath effect. The hall in which the measurement was performed had a metal roofing and there was grating on both of walls. Highly reflective EM environment may have affected the accuracy.

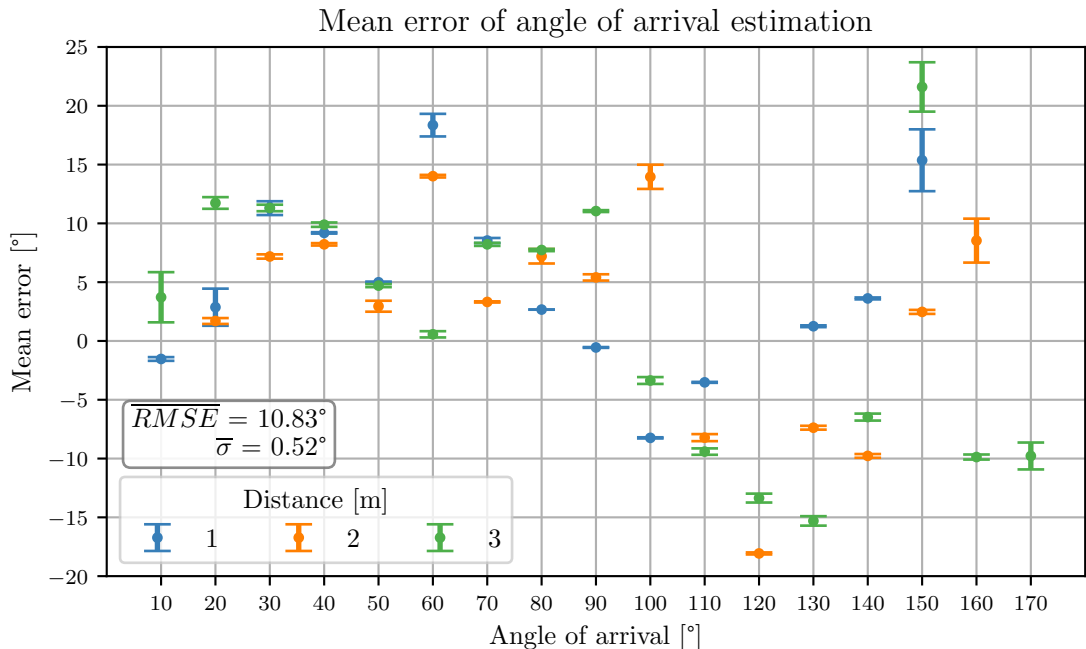


Figure 4.12: Mean error of AoA estimation – first series of measurements.

Second series of measurements was done in slightly different environment which was a local performance hall. Accuracy of algorithm was evaluated for distance of 2 to 5 m. Gathered results are shown in Fig 4.13. On the contrary to previous series of measurements, obtained accuracy of algorithm is much higher with mean RMSE of about 3.5° . The random high standard deviation of angle represented by error bars may have been caused by unfavourable multipath conditions which caused a substantial attenuation of signal received by one of the antennas. During the measurements signal levels varied and in some locations the difference was twofold in linear scale.

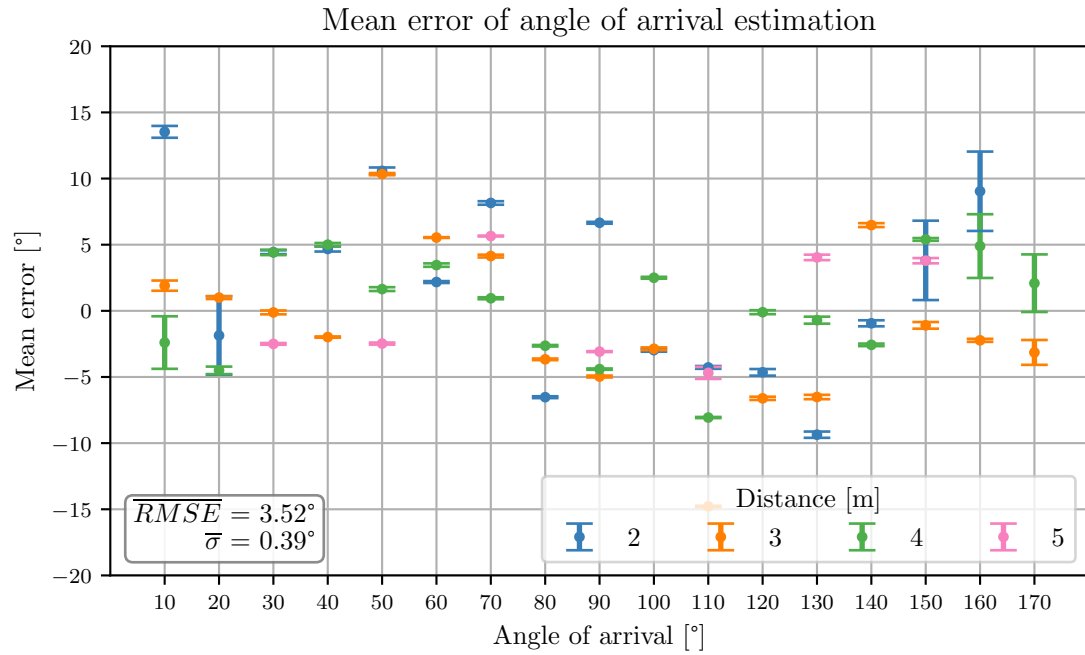


Figure 4.13: Mean error of AoA estimation – second room.

Chapter 5

Summary

5.1 Conclusion

Throughout the work MUSIC algorithm has been studied in numerous ways and tested within real radio environment. Performed simulations and sweeps of parameters presented how estimation of angle of arrival is affected by imperfections of construction and settings of the signal processing. Finally, field tests have been performed to evaluate the performance of algorithm with wireless phase calibration. Proposed method of synchronization of SDR front ends has been proven to be accurate and reliable.

Key findings of this work are as follows:

- Implementation of MUSIC algorithm with two receive nodes exhibits high susceptibility to multipath effects, which introduce an error in angle estimation. Even in scenarios where the distance between the source node and array was 2 times smaller than to any other obstacle, the error in form of constant offset remained. In some cases it was noted that position of the person performing the measurement affected the results returned by estimation.
- Precise wireless synchronization of phased array requires that there is no major crosstalk between the TX and RX parts of the setup and the antennas operate in far field regime. Otherwise the calibration will be biased and unreliable.
- Main component of distortion in both angle estimation and phase calibration was interference from other systems working in the same ISM band. Application of band-pass filtering enables to significantly reduce the value of error in both phases of the measurement. After this enhancement, presence of movement and effects of multipath propagation are sources of major errors in the system.
- It is safe to consider an overall accuracy of the constructed system as $\pm 10^\circ$ in line of sight scenario. However in some unfavourable conditions gross errors may occur.
- Performance of MUSIC algorithm is affected by series of parameters specified by both software and hardware environments. Array spacing, SNR level, snapshot size, shape of the array, characteristics of antenna and signal processing of obtained samples determine the results of the algorithm. Adapting these parameters to special needs of wireless systems may be a matter of optimization.

5.2 Future work

Having implemented an angle estimation system with two receive antennas and evaluated its results there are many topics to look into. Some of them may focus on extending the functionality of the array, improving the performance as well as tackling encountered problems and proposing novel solutions or applications.

Ideas for future development include:

- Increasing the number of antennas in the array and evaluating the properties of the expanded system. Implementation presented in this work enables easy extension of the array with additional USRP B210 serving as building blocks. Systems composed of 4, 8 or even 16 antennas are possible with use of Octoclock – clock distribution module produced by Ettus Research. Increase in the number of antennas may reduce the negative effect of multipath propagation on the results returned by the algorithm.
- Constructed angle of arrival estimation system can become a functional part of some of application like intelligent radio network employing directional transmissions. Systems properties may be investigated and modified to correspond to the needs of future mmW networks.
- Different array shapes may be constructed to extend the detection range to make the system more flexible and verify the obtained accuracy. Similarly omnidirectional antennas can be replaced with patch or more directional versions. In case of linear array directional antenna would help to reduce the ambiguity in regard to side of origin of the signal. Directional radiation pattern of antenna elements would probably also reduce the systems sensitivity to multipath propagation.
- More extensive testing of the setup in working conditions of the cellular radio head unit or wireless network access point may be beneficial to evaluate the system performance in possible deployment environment.
- Effects of differences in receiver sensitivity should be more broadly studied to verify how they influence MUSIC algorithm accuracy. If it would contribute to any major error in estimation then additional power calibration needs to be considered.

Acronyms

5G	Fifth generation technology standard for broadband cellular networks
ADALM	Analog Devices active learning module
AMV	Array manifold vector
AoA	Angle of arrival
API	Application programming interface
BS	Base station
D2D	Device-to-device
DB	Database
DoA	Direction of arrival
DSP	Digital signal processing
EM	Electromagnetic
EVD	Eigen-Value decomposition
FIR	Finite impulse response
FP	Fingerprinting
FPGA	Field programmable gate array
GPS	Global Positioning System
GPSDO	GPS disciplined oscillator
GR	GNU Radio
GUI	Graphical user interface
IoT	Internet of things
IQ	In-phase and quadrature
IRS	Intelligent reflecting surface
ISM	Industrial, scientific and medical frequency range
ITU-R	International Telecommunication Union – Radiocommunication Sector
LO	Local oscillator
LOS	Line-of-sight
LTE-M	Long-Term Evolution for Machines
M2M	Machine-to-machine
MAV	Moving average
MIMO	Multiple-input multiple-output
ML	Maximum likelihood
mmW	Millimeter Wave
MUSIC	Multiple signal classification
NLOS	Non-line-of-sight
P2P	Peer-to-peer
PLL	Phase locked loop

PoE	Power over Ethernet
QA	Quality assurance
RF	Radio frequency
RMSE	Root-mean-square error
RSS	Received signal strength
RSSI	Received signal strength indicator
RX	Receiver
SDMA	Space-division multiple access
SDR	Software-defined radio
SIMD	Single Instruction, Multiple Data
SNR	Signal to noise ratio
SWIPT	Simultaneous wireless information and power transfer
TDoA	Time difference of arrival
ToA	Time of arrival
TX	Transmitter
UE	User equipment
UHD	Ultra high definition
ULA	Uniform linear array
USB OTG	USB On-The-Go
USRP	Universal Software Radio Peripheral
VOLK	Vector-Optimized Library of Kernels

Bibliography

- [1] Z. Abu-Shaban, X. Zhou, T. Abhayapala, G. Seco-Granados, and H. Wyneersch. Error bounds for uplink and downlink 3d localization in 5g millimeter wave systems. *IEEE Transactions on Wireless Communications*, 17(8):4939–4954, 2018.
- [2] Ian F. Akyildiz, Shuai Nie, Shih-Chun Lin, and Manoj Chandrasekaran. 5g roadmap: 10 key enabling technologies. *Computer Networks*, 106:17 – 48, 2016.
- [3] Cisco and/or its affiliates. Cisco annual internet report (2018–2023). Technical report, Cisco, 2020. Available at www.cisco.com/c/en/us/solutions/collateral/executive-perspectives/annual-internet-report/white-paper-c11-741490.pdf.
- [4] Gaël Guennebaud Benoît Jacob. Eigen, a c++ template library for linear algebra: matrices, vectors, numerical solvers, and related algorithms. Available at http://eigen.tuxfamily.org/index.php?title=Main_Page#Credits.
- [5] Emil Björnson, Jakob Hoydis, and Luca Sanguinetti. Massive mimo networks: Spectral, energy, and hardware efficiency. *Foundations and Trends® in Signal Processing*, 11(3-4):154–655, 2017.
- [6] Ettus Research A National Instruments Brand. Phase synchronization capability of twinrx daughterboards and doa estimation. Technical report, Ettus Research A National Instruments Brand, 2016. Available at https://github.com/EttusResearch/gr-doa/blob/master/docs/whitepaper/doa_whitepaper.pdf.
- [7] Ryan Curtin Conrad Sanderson. Armadillo, c++ library for linear algebra & scientific computing. Available at <http://arma.sourceforge.net/>.
- [8] Junquan Deng. Doa-estimation-music-esprit. Available at <https://github.com/dengjunquan/DoA-Estimation-MUSIC-ESPRIT>.
- [9] Analog Devices. Adalm pluto customization and upgrade guide. Available at <https://wiki.analog.com/university/tools/pluto/users/customizing>.
- [10] Analog Devices. Adalm-pluto,software-defined radio active learning module. Available at <https://www.analog.com/en/design-center/evaluation-hardware-and-software/evaluation-boards-kits/adalm-pluto.html#eb-overview>.
- [11] Analog Devices. Fmcomms5 phase synchronization. Available at <https://wiki.analog.com/resources/eval/user-guides/ad-fmcomms5-ebz/phase-sync>.
- [12] Ericsson. Ericsson mobility report. Technical report, Ericsson, 2020. Available at <https://www.ericsson.com/4adc87/assets/local/mobility-report/documents/2020/november-2020-ericsson-mobility-report.pdf>.
- [13] E. Hossain and M. Hasan. 5g cellular: key enabling technologies and research challenges. *IEEE Instrumentation Measurement Magazine*, 18(3):11–21, 2015.
- [14] T. Izydorczyk, F. M. L. Tavares, G. Berardinelli, and P. Mogensen. A usrp-based multi-antenna testbed for reception of multi-site cellular signals. *IEEE Access*, 7:162723–162734, 2019.

- [15] M. Jokinen, M. Sonkki, and E. Salonen. Phased antenna array implementation with usrp. In *2017 IEEE Globecom Workshops (GC Wkshps)*, pages 1–5, 2017.
- [16] S. Monfared, T. Nguyen, T. V. d. Vorst, P. D. Doncker, and F. Horlin. Experimental demonstration of aoa estimation uncertainty for iot sensor networks. In *2020 IEEE 91st Vehicular Technology Conference (VTC2020-Spring)*, pages 1–5, 2020.
- [17] Qualcomm. Rising to meet the 1000x mobile data challenge. Technical report, Qualcomm Incorporated, 2012. Available at <https://www.qualcomm.com/media/documents/files/1000x-mobile-data-challenge.pdf>.
- [18] GNU Radio. Gnu radio website. Available at <https://www.gnuradio.org/>.
- [19] B. Rares, C. Codau, A. Pastrav, T. Palade, H. Hedesiu, B. Balauta, and E. Puschita. Experimental evaluation of aoa algorithms using ni usrp software defined radios. In *2018 17th RoEduNet Conference: Networking in Education and Research (RoEduNet)*, pages 1–6, 2018.
- [20] Ettus Research. B200/b210/b200mini/b205mini features. Available at <https://kb.ettus.com/B200/B210/B200mini/B205mini>.
- [21] W. Roh, J. Seol, J. Park, B. Lee, J. Lee, Y. Kim, J. Cho, K. Cheun, and F. Aryanfar. Millimeter-wave beamforming as an enabling technology for 5g cellular communications: theoretical feasibility and prototype results. *IEEE Communications Magazine*, 52(2):106–113, 2014.
- [22] V. C. Soon, L. Tong, Y. F. Huang, and R. Liu. A subspace method for estimating sensor gains and phases. *IEEE Transactions on Signal Processing*, 42(4):973–976, 1994.
- [23] Sergios Theodoridis and Rama Chellappa. *Academic Press Library in Signal Processing, Volume 3: Array and Statistical Signal Processing*. Academic Press, Inc., USA, 1st edition, 2013.
- [24] Srikanth Pagadarai Travis F. Collins. gr-doa: Direction finding in gnu-radio. Available at <https://github.com/EttusResearch/gr-doa>.
- [25] Srikanth Pagadarai Travis F. Collins. gr-doa: Direction finding in gnu-radio, 2017. Available at https://www.gnuradio.org/grcon/grcon17/presentations/gr_doa_gnuradio_direction_finding/.
- [26] Harry L. Van Trees. *Optimum Array Processing*. John Wiley & Sons, Ltd, 2002.
- [27] International Telecommunication Union. Imt vision –framework and overall objectives of the future development of imt for 2020 and beyond. Technical report, International Telecommunication Union, 2015. Available at https://www.itu.int/dms_pubrec/itu-r/rec/m/R-REC-M.2083-0-201509-I!PDF-E.pdf.
- [28] Isabelle Vin, Davy P. Gaillot, Pierre Laly, Martine Liénard, and Pierre Degauque. Overview of mobile localization techniques and performances of a novel fingerprinting-based method. *Comptes Rendus Physique*, 16(9):862 – 873, 2015. Radio science for connecting humans with information systems / L’homme connecté.
- [29] Marcin Wachowiak. Github repository containing gr-beamforming module. Available at <https://github.com/MarcinWachowiak/GNU-Radio-USRP-Beamforming>.



© 2021 Marcin Wachowiak

Poznan University of Technology
Faculty of Computing and Telecommunications
Institute of Radiocommunications

Typeset using L^AT_EX